POLITECNICO
MILANO 1863

SCHOOL OF INDUSTRIAL AND INFORMATION ENGINEERING

MASTER OF SCIENCE IN
SPACE ENGINEERING

Investigation about the free volume in butadiene and isoprene based elastomers by Positron Annihilation Lifetime Spectroscopy

Supervisor: prof. Giovanni Consolati

Author:

Giuseppe Maria Viola

883457

Academic Year: 2019-2020

Contents

List of Figures

List of Tables

Abstract

The aim of this thesis is to study the free volume fraction in a set of elastomers. This quantity is an important parameter for the understanding of their mechanical and transport proprieties. The study is focused on trying to find the best shape for the cavities that could fit the most the experimental behavior of each polymer. The experiments were carried on five different rubbers blends characterized by a different percentage of the main components, butadiene and isoprene. Systematic discrepancies were found using the standard spherical approximation, so the focus was put on different geometries, in particular on elongated/flattened cylindrical shape.

Chapter 1

Introduction

The present work bases its hypothesis on the results obtained from the studies of a isoprene rubber and its miscible blends [1]. In that paper, it was obtained the free volume fraction in function of the temperature. The authors of the study used the same investigation technique employed in this work, that is the Positron Annihilation Lifetime Spectroscopy. Thanks to PALS the authors found an excellent agreement with the theoretical free volume fraction, but in order to do that, they had to introduce an ad-hoc occupied volume that did not correspond to the one predicted by the theory. On the other hand, making use of the theoretical occupied volume, it could be noticed a discrepancy between the two free volume fractions. Therefore, starting from this premise, the aim of this work is trying to understand if this systematic discrepancy may be due to other assumptions, implicit in the studies involving positronium. Indeed, it is possible to correlate the average lifetime of the positronium, coming from the experiment, to the dimension of its host cavity (that represents the free volume) by adopting a mathematical model framing its geometry. The most diffuse representation of these cavities is through a spherical geometry. Due to the discrepancies with the theory, in this work another geometry has been examined, the cylindrical one, in order to better characterize the cavities of a series of isoprene and butadiene elastomers. It was found, in this case, a very good agreement between experimental and theoretical data, as long as the growth of the cavities with the temperature was not assumed isotropic but was considered to rise faster in the direction of the radius of the cylinder rather than in its height.

It was chosen to make use of the PALS analysis since it is one of the few experimental techniques able to supply information about the free volume in a polymer. The free volume is a fundamental parameter since it is strictly connected with important characteristics of the polymer such as mechanical and thermal properties. In comparison to other methods, PALS has the advantage of not interfering with the matter subjected to study, moreover it does not need to use large probes that could influence the evaluation of the free volume.

PALS uses Positronium (Ps), that is an unstable system formed by an electron and its antiparticle, a positron, orbiting around their common center of mass. It forms when a positron is injected into a medium and interacts with the surrounding electrons, placing itself into the cavities of the material. In polymer research the interest is focused only on ground state Positronium which exists in two sub-levels, according to the spin orientations of the two particles, para-Ps (p-Ps) and orto-Ps (o-Ps). Since positrons and electrons are antiparticles, they annihilate transmuting their mass into pure energy, not leaving behind any waste and this is optimal for the study of free volume holes. In vacuo the p-Ps annihilation process happens with the emission of two γ rays and its lifetime can be approximated by the following formula [2]:

$$t_0 = \frac{2\hbar}{m_e c^2 \alpha^5} = 0.1244 \text{ ns.}$$
(1.1)

While the o-Ps annihilate emitting three γ rays and the time of decay can be approximated as follow [2]:

$$t_1 = \frac{\frac{1}{2}9h}{2m_e c^2 \alpha^6 (\pi^2 - 9)} = 138.6 \text{ ns.}$$
(1.2)

Thus, p-Ps lifetime is approximately 125 ps, this time span is too short to be useful for the purposes of this research, moreover it does not vary significantly with the host cavity size. On the other hand, o-Ps has a lifetime of about 140 ns, three orders of magnitude higher than the p-Ps and more importantly it undergoes another process consisting in the

annihilation in two photons with an electron of the surroundings in a relative singlet state. This shortens the lifetime of the o-Ps with respect to its value in vacuo, the smaller the cavity the shorter its. lifetime. This phenomenon is exploited to relate the experimentally estimated lifetime of o-Ps with the size of the sub-nanometric holes v_h of the material under study, provided that the o-Ps lifetime is shorter than the one of the cavities. Indeed, these last have to be thought as dynamical entities, which are generated and disappear according to the movement of the macromolecules.

Of course, for different choices of shape, different mathematical model will be adopted and so different volumes for the holes will be obtained. In reality the cavities have an irregular shape so any geometry chosen would be a mere approximation, nonetheless the key point of this research is focused on this aspect since among the various possible geometries, only the most appropriate one will give reliable insight about the morphology of the nanostructure of a polymeric material. The simplest approximation is the spherical one but as it will be shown further on, this geometry does not match with the theory. Moreover, info about the behavior of the specific volume V_s of the polymer with temperature are available from dilatometry studies.

Both the volume of the cavities v_h from the PALS analysis and the specific volume V_s from dilatometry are needed to obtain the number density of holes N in the polymer and the occupied volume V_o, by means of a linear interpolation of V_s versus v_h both at the same temperature. At this point it can be calculated the specific free volume V_f that will be in turn used to get eventually to the free volume fraction f (all these steps will be seen in detail in a dedicated chapter). As the name says, this parameter represents the portion of the free volume on the entire volume, it is the synthesis of all the previous results, and it allows to compare easily the experimental data with the theoretical ones.

Of course, a theoretical model must be introduced to compare the obtained results with. In this work it has been chosen to make use of the *Simha-Somcynsky* lattice-hole theory [3]. This is a theory that describe amorphous polymer through two equations of state that relate various quantities as the reduced specific volume and the free volume fraction h with the corresponding reduced temperature (all these other steps will be

explained in detail in a dedicated chapter too). Then, these general results can be adapted to the particular polymer under study by means of appropriate scaling parameters T^* and V^*. Once these scaling parameters are available it is possible to link the theoretical free volume fraction h with the absolute temperature chosen for the study and finally it can be compared to the one obtained experimentally f and see if they match or if there are discrepancies.

This research was conducted on the following elastomer blends:

1. S1= Europrene Neocis BR 40 + 3phr DCP (1.2 pure) – Butadiene rubber
2. S2= IR high cis type IR0310 Keaton + 3phr DCP (1.2 pure) – Isoprene rubber
3. S3= 50% S1 + 50% S2
4. S4= 25% S1 + 75% S2
5. S5= 75% S1 + 25% S2
6. S6= NBR N4560 + 3phr DCP with 45% of acrylonitrile

As it can be seen, at each elastomer was assigned, for convenience, a label "Sx". From now on the elastomers will be indicated according to this nomenclature. In the following table are listed, for each polymer, the parameters useful for this work.

<div align="center">

Table 1 - Data on the elastomers

</div>

	S1	S2	S3	S4	S5	S6
Density at 296K [g/cm³]	0.93	0.91	0.92	0.91	0.92	1.01
T_g [K] - DSC	166	215	215	215	214	265
UTS [N/mm²]	2.0	1.50	1.62	1.35	1.40	2.30

The elastomer S1 was not object of study during this work, it is here reported only because it is part of the other elastomer blends.

In the next chapters it will be described how the experimental data are obtained, how they are elaborated, how the spherical geometry fails to match theory results and how other shapes are a better fit to frame the holes.

Chapter 2

Acquisition Chain

Positronium Annihilation Lifetime Spectroscopy

Before focusing on the various acquisition instruments one by one, it is important to describe the fundamentals of the PALS, since it is our main tool of investigation. Thus, a more detailed description about positronium is needed, starting from its formation.

Positronium is formed by a positron and an electron. For this work positrons were generated by the natural decay of the radioisotope ^{22}Na. It undergoes to the so called β^+ decay, emitting a positron, a γ ray and an antineutrino. Positrons are emitted with a continuous range of kinetic energy between 0 - 520 keV and within 2-3 ps it is emitted a γ ray with an energy of 1.274 MeV. Since the time scale of the measurements of interest is in the order of magnitude of several ns, the emission of positrons and the γ ray can be approximated as simultaneous, so that the positron emission could be identified by detecting the photon. The positrons are emitted into the polymer under study that has an ionization energy of about tens of eV, much lower than the one of positrons. A positron injected into a material loses its energy due to anelastic collision with molecules which are ionized. The positron leaves behind a trail of unpaired electrons which rapidly recombine with their ions. Only when the positron has lost enough energy the positronium can form.

Positronium is an unstable system that decays emitting γ rays. The ground state positronium can be subdivided into two sub-states depending on the spin orientation of the electron and the positron forming it. There is the state called para-Ps when their spins are anti-parallel, and the state called orto-Ps when their spins are parallel. In vacuo p-Ps decays emitting two γ rays and its lifetime is about 125 ps while o-Ps decays emitting

three γ rays and its lifetime is about 140 ns, so there are three orders of magnitude between them. While in a material, due to the presence of surrounding electrons, the positronium system can also annihilate with an electron of the medium through the so called "pick-off" process. Various situation may happen depending on the spin state of the positron of the Ps atom and the electron of the material. Regarding the positron of a p-Ps atom (anti-parallel spin) can interact with an electron of parallel spin forming an o-Ps atom, but this slightly affect its annihilation process since it is much more likely that the positron of the Ps annihilate with its own electron since the process is much faster, as it was stated before. Thus, almost nothing changes for the p-Ps moving from vacuo to matter. The situation changes as far as o-Ps is concerned. If a positron of an o-Ps atom encounters an electron with parallel spin state, again, nothing changes, since the annihilation lifetime would be of the same order of magnitude. If, on the other hand, it interacts with an antiparallel state electron it will decay into two gammas, decreasing up to three orders of magnitude the process. In a medium with a density comparable to the one of a polymer, the o-Ps decreases its lifetime from about 140 ns to about 2 ns, so it is greatly affected by moving from vacuo to matter and in addition its lifetime it is strongly correlated to the dimension of the cavities. This happens for a non-magnetized material where half of the electrons have a spin up and the other half have a spin down so that o-Ps annihilates half of the times as p-Ps and the other half as o-Ps. While if the material is very porous, the "pick-off" process is negligible.

In the next chapter it will be seen that the spectrum was deconvoluted in three components following this annihilation scheme. The shortest one, of about 0.12 ns, represents the annihilation of p-Ps, the middle one, of about 0.3-0.4 ns, represents the annihilation of the free positrons in less-dense areas of the material and the last component, of about 2-3 ns, represents the o-Ps annihilation (that is three time more probable than the p-Ps) through the "pick-off" process and it's much longer than the others.

The information to be acquired from the spectral analysis is the lifetime of these three different components with a particular care for the longer one since it is the one

dependent from the hole size. In order to have this information it has to be measured the time interval between the positron emission, that, as it was shown, can be represented by the start γ ray that coincides in first approximation with the positronium formation, and the stop γ ray of the annihilation process. As highlighted before, the most probable way for positronium to decay is with the emission of two γ rays, thus, there will be two stop photons. It is known that the starting photon has a fixed energy of 1.274 MeV, typical for the β+ decay of *22Na*. Now it has to be derived the stop photon energy. Since the positron and the electron in the positronium bound state are antiparticles, they annihilate completely, so the involved energy is given by the mass-energy equivalence equation $E = 2m_ec^2$, with m_e the mass of the electron that is equal to the one of the positron, considering also that the positronium atom is in thermal equilibrium with the surrounding material and it has negligible kinetic energy. Thus, the two photons have the half of the total energy released, that is 0.511 MeV. The big gap in the start and stop photon energies helps their discerning and leads eventually to the measurement of the time interval between them and so to the lifetime. This final step is done considering that annihilation events distribute according to the radioactive decay law:

$$n(t) = n(0)e^{-\frac{t}{\tau}}$$

(2.1)

where *n(t)* is the number of atoms of positronium at the time instant *t*, *n(0)* is the number of atoms of positronium at the time instant assumed as zero, *t* is the measured elapsed time between the start and stop photons and finally τ is the average lifetime we are looking for.

Scintillator

Scintillators are used as nuclear radiation detector thanks to their peculiar characteristic of exhibiting scintillation, that is a photoluminescence process triggered by ionizing radiation. It consists in the absorption of a γ ray photon's energy and the subsequent energy emission in the form of visible light or UV radiation. When a photon collides with a scintillation crystal brings its molecules to an excited state, then these molecules return back to the ground state by emitting photons with a higher wavelength and so lower energy with respect to the original one. To have luminescence the material has to be made so that the optical transition between excited and ground state is allowed, otherwise the incoming photon would go through the crystal without triggering the absorption-emission process described before. Moreover, it is required that the excited state time isn't higher than 10^{-8} s, which corresponds to the typical lifetime of an excited state for an allowed transition. Thus, all the substances that get excited to metastable states are excluded since their excited lifetime is significantly longer (in the order of 0,01-1 s) and the probability of a spontaneous transition to a lower energy level is decreased by a factor of 10^6 to 10^8. There are two main type of scintillators, the organic scintillators and the inorganic ones.

Inorganic scintillators are crystals grown in high temperature furnaces and are typically Alkali Halides, Oxides or Lanthanium Halides. They have scintillation properties by virtue of their crystalline structure, that creates the energy bands between which electrons can jump. In a pure inorganic crystal lattice such as *NaI*, electrons are only allowed to occupy selected energy bands. The forbidden band or band gap is the range of energies in which electrons cannot be found. The absorption of energy can elevate electrons from the valence band to the conduction band leaving a gap in the valence band. However, the return of an electron to the valence band with the emission of a photon is an inefficient process. Few photons are released per decay, the energy is emitted by other mechanisms. In addition, band gap widths in pure crystals are such that the resulting emitted photon is too high to lie within the visible range.

Small amounts of impurities are therefore added to the crystal. The impurities are called activators, they create special sites in the lattice at which the band gap structure is modified. The energy structure of the overall crystal is not changed, just the energy structure at the activator sites.
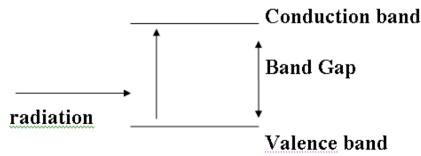
Figure 2.1 - Pure Crystal   **Figure 2.2** - Activated Crystal
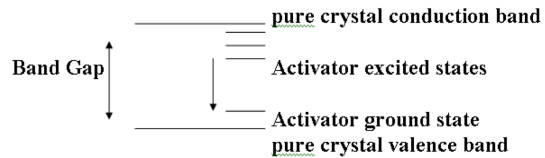
There are now new energy states within what would be the forbidden band in the pure crystal. The electron can de-excite through these levels back to the valence band. The energy levels created by the activator's presence within the crystal are narrower than in the pure crystal. This greatly enhances the efficiency of the inorganic crystals, moreover the photons emitted will be lower in energy, thus the emission spectrum is shifted to longer wavelengths and will not be influenced by the optical absorption band of the bulk.

Organic scintillators on the contrary are composed of aromatic hydrocarbons, unlike inorganic scintillators, they scintillate on a molecular level. No crystal structure is needed. Basically, each scintillator molecule can act as a scintillation center. Their photoluminescence process is based on the *Stokes-shift* effect, where a system decreases its energy after a photon absorption by emitting another photon with lower energy, and this is the phenomenon that transforms the start and stop γ photons in visible and UV photons detectable by the photomultiplier. This phenomenon is due to the fact that excited states and ground states have different interatomic distances so once a photon is absorbed, molecular state is excited to a certain vibrational level of the excited electronic level, this transition is followed by a decay to the lower vibrational level and finally there is a transition back to the ground electronic state, but in a higher vibrational state (**Figure 2.3**).
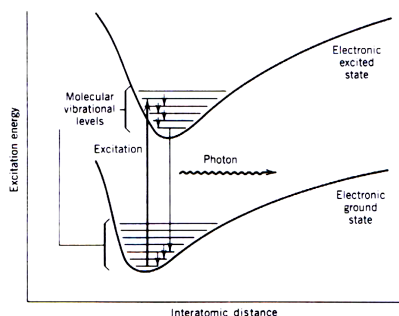
Figure 2.3 - Energy levels of organic molecules

There is a substantial difference between absorbed and emitted photon energy, the missing energy has been thermally dispersed in the scintillation crystal. The energy level scheme explains why organic scintillators can be transparent to their own fluorescence emission. Most fluorescence emissions have a lower energy than the minimum required for absorption. There is little overlap between emission and absorption spectra, therefore the emitted light mostly passes straight on through the scintillation medium, this is important since afterwards it must reach and transfer its energy to the photocathode.

Apart from their structural differences, inorganic and organic scintillators differ in their mode and level of interaction with ionizing radiation. For a typical x-ray/γ-ray energy range from 10 keV up to 1 MeV, the main interaction mechanisms involved are the Photoelectric effect and Compton scattering. In order to express numerically the probability that an atom will cause a photon of a given energy to undergo either one of these two process, it is introduced the concept of cross section. The total absorption cross section, for removing a photon from the impinging beam of light per atom, is given by the sum of these two processes.

The Photoelectric effect is a radiation-matter interaction process involving a photon impacting with an atom in such a way that its energy is absorbed, and in exchange, an electron is expelled. The kinetic energy of the electron expelled is equal to the one of the impinging photon minus the binding energy. It come by itself that not all kind of radiations are enough to trigger this phenomenon, they must have at least an energy equal to the binding energy of the electron. Moreover, the higher is the frequency (and so the energy)

of the photon, the higher will be the probability of expelling the electron. In this case the cross section is proportional to Z^5, with Z the atomic number of the atom.

The Compton effect is a scattering process due to the interaction of a photon with a charged particle, an atomic electron in this case. The γ-ray is not completely absorbed, only part of its energy is transferred to the recoiling electron, resulting in a decrease in energy of the photon, that is scattered out of the beam. In this case the cross section is proportional simply to Z.

There is also another effect called pair production process in which a positron and an electron pair are created with a total energy equal to the one of the photon. This can happen only when the energy in play is higher than $E = 2m_ec^2$ = 1,02 MeV, that is the sum of the rest mass of the to particles. Actually, in order to have a significant absorption coefficient, the photon energy has to be much higher than 1.28 MeV, that is the start photon energy and the maximum energy dealt with in this work, so this term is simply neglected.

Inorganic scintillators are usually made of high Z-elements and have a fairly high density, the high Z make the photoelectric effect the predominant process (it depends on Z^5) over the Compton effect (it depends on Z), while the high density increases the interaction efficiency. On the opposite, organic scintillators are made of low Z-elements and have low density. The main interaction in this case is the Compton scattering and because of the low density, more volume is required to obtain a reasonable detection efficiency.

For this work it has been chosen inorganic scintillators, because it can be easily distinguished the photoelectric peaks over the Compton contribution, so that the energy windows can be centered around the peaks, in order to obtain an increased efficiency and a lower background by making the window smaller. The inorganic scintillators used are quite big (10 mm diameter, 40 mm height), this worsen the resolution function, but it is still acceptable because the focus is mainly on the o-Ps lifetime which is longer than the FWHM of the resolution function. In organic scintillators the energy peaks are not as

well defined, thus they need larger energy windows and have a lower efficiency, but they excel in the response time that is very short. In order to overcome the problem of the usual high response time of inorganic scintillators (that is of about 0,1 ms) it was used the *BaF₂* crystal, that compared to *NaI*, one of the most diffused inorganic scintillators, has a response time much higher, its fluorescent time is of about 1 ns, but it has a lower efficiency, even if it still has energy spectra with well defined energy peaks.
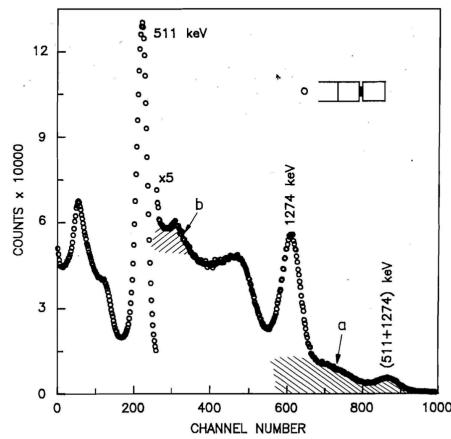
Figure 2.4 - Energy spectrum of BaF₂ scintillator

The usual geometry for the detectors is face-to-face, the two scintillators are disposed as close as possible and in between them there is the copper cup containing the sample and the *²²Na* positron source embedded in two Kapton foils. The start photon has an energy of 1,274 MeV and the two stop photons have an energy 0,511 MeV, as was stated before. Thus, in the lifetime measurement, the energy windows are set at 1,274 MeV and 0,511 MeV full energy peaks that are well visible in **Figure 2.4**.

The region highlighted with the letter *a* in the figure denote an area where the 1,274 MeV start photon and the 0,511 MeV stop photon sum their spectra, this happens when the solid angle subtended by the start oscillator reach 2π and so one of the two annihilation γ-ray must enter that scintillator. Since almost all the positrons do not survive for more than few nanoseconds in a solid, they live for sure less than the risetime of the photomultiplier and so they are accounted as one event. While the region highlighted

with the letter *b* represent the region where the stop photon energy of 0,511 MeV is accounted together with the backscattering.

The registered time intervals between the full energy peak at 1,274 MeV and the one at 0,511 MeV are the undistorted time intervals, the so called "good events" where start and stop signals are correctly accounted for. But with the linear geometry described above it can also happen that other distorted time interval could be registered. For example, the scattering of the 1,274 MeV photon in the scintillator at an angle over 66°, when combined with the energy of the annihilation photon (region *a* in the **Figure 2.4**), gives to the recoil electron an energy sufficient to trigger the start. Or going on, if the Compton effect in the start counter scatters the γ-ray backwards, this enters the stop counter summing up with the 0,511 MeV photon (region *b* in the **Figure 2.4**) altering the stop count.

The Constant Fraction Discriminators (CFD) produce timing signals when the bipolar pulse crosses zero. When the pulse is the sum of two signals, the delayed component of the sum delays the moment of zero crossing. In this way, the sum of spectra alters the measured intervals. In the first case listed, the start signal is delayed by a time proportional to the lifetime of a positron, while the stop signal is accounted correctly, so it adds a spurious component of smaller lifetime with respect to the "good event" case. While in the second case listed, both the start and stop signals are delayed, the distorted time spectrum in this case is more complex, but again it can be seen a short-life component. Placing about 6 mm of Lead (*Pb*) in front of the start counter helps in reducing the spurious component, since this act as a filter absorbing almost all the backscattering photons and reduce the intensity of the region *a* in the start counter, but at the same time this procedure decreases a lot the counting rate. For this reason, the linear (180°) geometry is not acceptable in the positron lifetime measurement with BaF_2 scintillators. The solution adopted was to place the two counters forming an angle of 90° so that only one of the pair of annihilation photons is able to enter the scintillators.

In order to evaluate the scintillator efficiency, it is considered an impinging photonic beam with power P_n. Then are accounted all the phenomena interfering with the detection process. The power produced by a scintillator is:

$$P_{sc} = P_n F_n C_{np} \qquad (2.2)$$

where F_n is the fraction of total energy absorbed by the scintillator, C_{np} is the conversion efficiency of a γ ray in visible or UV ray. A fraction of P_{sc} is lost across the scintillator, and the power effectively emitted is:

$$P_{sc}^e = P_{sc} T_p F_p \qquad (2.3)$$

where T_p is the degree of transparency of the scintillator to its own radiation, and F_p is the fraction of photon actually emitted. Thus, the scintillator efficiency become:

$$\eta_{sc} = F_n C_{np} T_p F_p \qquad (2.4)$$

resulting:

$$P_{sc}^e = \eta_{sc} P_n \qquad (2.5)$$

Photomultiplier

After the γ-rays, produced by the β⁺ decay, are transformed into visible light, the photonic signal has to be converted into an electric one. For PALS it is commonly used a quantum photodetector, capable to identify an incoming photon. The detector can work by either one of these two effects: photon energy can be used to excite an electron in a semiconductor from valence band to conduction band causing a conduction enhancement, or to extract the electron from the material. In both cases detection is a threshold process, meaning that there is a minimum energy to be reached by the photons

in order to have an effect on the electrons. In this work it was used the external-effect photodetection.

A standard detector of this kind is the vacuum photodiode. It is formed by two plates at a certain distance d in vacuum, with a strong electric field ε among them. The photon colliding with the cathode (the plate with negative potential), that has an energy quantified by the equation $E=hv$, in order to extract an electron by photoelectric effect, has to satisfy the following threshold condition:

$$hv > e\phi \qquad\qquad (2.6)$$

where ϕ is the work function of the cathode material (i.e. the minimum energy required to extract an electron). If this happens, the electron extracted is accelerated towards the anode by the electric field. The current generated by this charge movement act as electrical signal that reveals a photon arrival. The signal produced is weak and need to be amplified, but the background noise introduced by these amplifications is higher than the one of the photodetector alone. Thus, in order to increase the signal-to-noise ratio, a photomultiplier (PM) was used in this work.

In a photomultiplier other than the initial cathode and the final anode, there are also a series of intermediate electrodes, called dynodes, polarized with increasing potential. Electrons extracted from the photocathode, before arriving to the final anode, collide first with the dynodes. The electrons, accelerated by a strong electric field, acquire enough energy to extract a certain number of secondary electrons from the first dynode, which are accelerated towards the second dynode extracting more electrons and so on in a multiplication effect, as shown in the following figure.
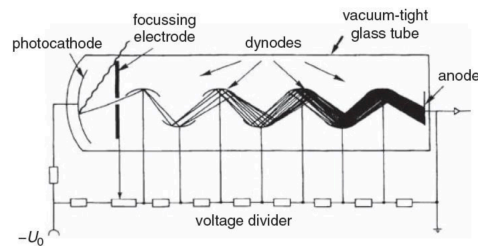
Figure 2.5 - Working principle of a Photomultiplier

Since the electrons emitted from the photocathode need to have enough energy to generate further secondary electrons, the threshold condition must be greatly exceeded, it must occur that the residual energy of an electron extracted by a photon must have a residual energy $E = h\nu - e\phi \gg 0$ (from **eq. 2.6**).

The photomultiplier gain can be defined as $G = \alpha^n$, where α is the average number of secondary electrons produced by every dynode and n is the number of dynodes. The number of electrons reaching the anode plate is proportional to the gain G and the so is for the electric signal produced. The stochastic nature of the multiplication process introduces another kind of noise due to the gain fluctuations. The photomultiplier is intrinsically a nosier device than the vacuum photodiode, but it has the great advantage of avoiding the electronic amplification step, ending up with an overall better signal-to-noise ratio. The typical voltage supply value of a photomultiplier varies in the interval 1.8-2.2 kV, to be distributed among the two main electrodes and the dynodes by means of a voltage divider. Since the dynode gain G shows a saturation behavior for a certain voltage V (about 250 V), it means that it is not significant any further. Usually, only the first stadium is polarized up to saturation voltages because a missing electron at this step, implies a big variation of the number of electrons arriving to the anode (because of the multiplication effect), whereas a missing electron at the final step is not so important since it weighs less on the overall process.

The photomultiplier efficiency can be defined as:

$$\eta_{pm} = S_m f F_c \qquad (2.7)$$

where S_m is the cathode spectral sensibility, it represents its dependance on the incoming photon wavelength, f represents the degree of overlapping between the spectrum actually produced by the scintillator and the cathode spectral sensibility, F_c is the fraction of photoelectrons collected by the dynodes.

As stated before, the electrons are eventually collected by the anode in a region that it would better to be dot-like and placed at its center. But there are also electrons collected at the anode edges that need to reach the center causing a broadening of the system impulse response. In fact, secondary electrons could be emitted along directions not perpendicular to the dynode, colliding with the next one in peripheral areas. Moreover, even if electrons would be emitted along the axis of the detector, impinging photons could be collected by peripheral areas of the photocathode and there would be electrons reaching the anode far from its center anyway. These two factors restrict the temporal resolution of the photomultiplier. In order to focus the incoming photons to the photocathode center cathode dimensions can be reduced, but this operation would decrease the detection efficiency. The electronic beam could be confined around the detector's axis, focusing electrons through electrostatic field gradients, using crossed magnetostatic and electrostatic field or it could be done simply using a geometrical focalization by means of dynodes with spherical cap. While the Photomultiplier response time is a negligible parameter in the case of PALS since the same delay concerns both start and stop detectors thus it is irrelevant in relative temporal measurement. However, the maximum delay of the response time is given by the time needed by an electron, moving along the axis, to cross the entire length of the photomultiplier, from the photocathode to the anode.

For this work **PHILIPS XP 2020 phototubes** were used. Voltage supply is 2300 V, with a corresponding gain of about $3 \cdot 10^7$, and it is distributed among various dynodes by a suitable divider, in particular it is concentrated between the photocathode and the first

dynode. As a voltage supplier an **HV ORTEC 556** was employed. Impulse rise time at the anode is about 1.8 ns. Average transit time of electrons through the phototube is about 30 ns, but the real important parameter is its dispersion valued around 250 ps.

CFD

The Constant Fraction Discriminator (CFD) is a device used to distinguish start and stop events and to produce fast synchronizing signals to be used to measure the positronium lifetime. CFD intercept input pulses coming from the anode of the photomultiplier in the range of 0 to -10 V and if they exceed the lower bound, but not the higher one, within 10 ns after the constant fraction zero crossing time, then the CFD generates a timing output signal. As it was shown before, a photon incident on the photocathode that satisfies the threshold condition generates a current pulse at the anode, the amplitude of this current is proportional to the impinging photon energy. This is why it is possible to distinguish a start photon from a stop photon.

To correctly report start and stop photon, the energy windows of the instrument must be calibrated. On the stop detection branch, they must be calibrated so that only pulses corresponding to photon energies around 0.511 MeV are selected, whereas on the start detection branch only pulses corresponding to photon energies around 1.274 MeV. When suitable window energy amplitudes have to be chosen, it can be decided if they should cover a narrower or a wider interval. A narrower interval means less background and higher resolution but at the same time less counts per unit time and this is a disadvantage since in order to have the same counts (for a batter statistic) measurements must be longer worsening the resolution function due to possible drifts induced by thermal fluctuations. In this work the windows are calibrated so that are accepted only stop signals having energy in the range ± 20% of 0.511 MeV energy peak and are accepted start signals having energy higher than 70% of 1.274 MeV energy peak. The stop channel has an energy window with a lower and an upper bound in order to exclude both low energy photons, due to background noise, and high energy photons related to the start signal. Thus, the energy window for stop signals has to be quite narrow in order to

minimize false stop signals that in reality are degraded start signals, but not too much in order to keep a good counting rate. While, for the start signal is simply enough a lower band that cuts out the low energy photons to not misinterpret stop signals.

Here it is described how energy windows are calibrated in practice. The electrical output from the anode is sent to the CFD, then to the ADC and finally to a computer. If no bunds are set, on the monitor is possible to see the whole spectrum on a graphic in which x and y axis represent respectively the channel number (proportional to the energy released by the scintillator) and the number of counts at a certain energy. Using two markers a lower and an upper bound are set for the stop energy windows. Then, it is taken the same signal as before but coming from one the last dynodes, it is amplified and sent to the ADC where a coincidence circuit generates an output only when it receives the same signal from both the discriminator and one of the last dynodes. Therefore, what it is now displayed on the monitor is the coincidence between signals coming from the dynode and signals filtered by the CFD. Having kept fixed the markers position, precision potentiometers, located in the front panel of the CFD, can be used in order to determine lower and upper levels so that the monitor would show only the part of the spectrum within the markers set before, and finally energy window bounds can be set. The same procedure is repeated for start signal. Usually, energy windows calibration is conducted periodically in order to take in account unavoidable parameters drifts of electronic instrumentation.

Once energy windows are set, the focus is put on the time lag between the start event and the stop one, that is of fundamental importance since it regards the accuracy of calculation of the lifetime of positronium. The discriminator is able to supply very fast logic pulses temporally correlated with the anode signal, allowing to indicate with a very high precision when a start or stop event occurs. But the generation of these signals is affected by several error sources. There could be signal distortions, due to the stochastic nature of the detecting process, like variations in the photon production rate in scintillators or fluctuations in photon and electron transit time respectively in the scintillator and the phototube. Temperature variation in the measurement environment

is usually also a problem since it produces temporal drift in the measure, but this was not a problem for this work since it was carried out in a thermo-regulated laboratory, with a variation in temperature of maximum ±1° in a day with measures lasting at maximum 24 hours. The most troublesome problem is the *amplitude walk*, that is the systematic dependence of the time marker on the amplitude of the input pulse. This problem can be solved by obtaining a *constant fraction* pulse. The unipolar incoming signal is split in two signals, one of which is attenuated by a factor f, whereas the other one is delayed and reversed; the two modified signals are then summed, making a bipolar pulse, this is the *constant fraction* pulse. By optimizing parameters like the delay undergone by the signal in one branch and the attenuation undergone by the other one it is possible to create a pulse whose zero-crossing point is independent from the original pulse amplitude (**Figure 2.6**). Optimization is accomplished inserting suitable delays on input signals. This an empirical procedure and after several trials of different delays on the stop branch and the start branch, the couple providing the best resolution is the one adopted.
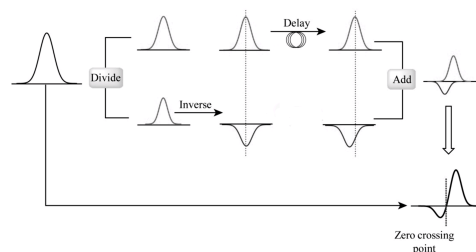
Figure 2.6 – Working principle of a CFD

For the stop channel were used the **CFD ORTEC 583** device, and the **CFD ORTEC 473A** device for the start channel. The last one is characterized by only one boundary, the lower one and this is enough given what was said before, while the other one has a real energy window and let to set both the lower and the upper bound.

TAC

The Time to Amplitude Converter is a module that measures the time interval between start and stop input pulses and generates an analogical output pulse proportional to the measured time. The time can span from 50 ns to 2 ms and a start-stop conversion is carried out only when a valid start has been identified and a stop pulse arrives within the selected time range. TAC bases on the working principle of an RC integrator circuit. When a valid event is identified on the start channel, i.e. a pulse overcomes the CFD selection and gets to the TAC, at the same time that the timing pulse is generated by the discriminator, the RC circuit is fed by a current supply. This kind of circuit generates a ramp function as output when it receives a step function as input. If within a prefixed temporal window, a pulse overcomes the CFD selection on the stop channel, then, correspondingly to the timing pulse coming from the stop discriminator, the input to the RC integrator is disconnected and the time elapsed between the two events can be calculated from the height reached by the ramp. In an RC circuit the two quantities, voltage and time, are directly proportional each other, linked by the following relation:

$$v_{out} = \frac{v_{in}}{RC}t$$

(2.8)

Usually, TACs show some non-linearities at the initial stage of the charging process of the capacitor and so the relation between voltage and time could not be approximated anymore as linear. In order to solve this problem and to keep using the linear relation **2.8** to calculate backwards the elapsed time, an artificial delay is inserted on the stop channel by means of a suitable cable, so that all the measured time intervals appear to last more (a start and a stop photon received simultaneously would give rise to a lifetime equal to the additional delay). The consequence of this operation is a rigid translation of the spectrum on the time axis. If no stop input is accepted before an overrange condition is sensed (usually within 50-100 ns), the measurement will be aborted and no output signals for the TAC will be generated. If no stop signal is identified within a prefixed time interval from the start pulse, it is assumed that the stop photon (0.511 MeV) has not been detected, so the ramp is reset, and the TAC is set up to wait another start signal. If the

TAC didn't contemplate this occurrence, TAC terminal voltage would continue to increase until a stop pulse is detected, but almost certainly it would be related to another start photon, leading eventually to a misleading lifetime. In the present work was used a **TAC ORTEC 566**.

ADC

The Analog-to-Digital Converter is needed to transform the analogical output coming from the TAC into a number proportional to it, so it can be read by a computer. The converter used in this work performs a ramp conversion. A digital circuit compares the analogical value to be converted with the output of a circuit generating a ramp, a kind of integrator similar to the one seen in the TAC. The comparator produces a *high logic* output only when the ramp overtakes the analog voltage to be converted. This logic output is linked to a counter that stores *clock pulses* at constant frequency, until a commutation from *low* to *high* occurs, the number of counts is proportional to the analogical value to convert and represents the number produced by the conversion. The most significant parameters for an ADC are its response speed and its integral and differential linearity. The conversion speed is directly related to the time interval during which any new arriving signal is not accounted for since the ADC is already busy in converting the previous one. The maximum dead time is corresponding to the highest voltage coming from the TAC. The conversion linearity is an index of how much the digital output is actually proportional to the analogical input amplitude. Ideally, the input-output curve of an ADC is a series of steps, so that linking the middle points of each step gives place to a straight line. In practice that does not happen. Thus, it is useful to define the integral linearity parameter, as the maximum deviation between the ideal straight line and the real curve, and the differential linearity, as the difference between two contiguous digital values, that should be ideally constant.

A converter **AD SILENA 7411** was employed for this work, with an integral linearity lower than ± 0.025% and a differential linearity lower than ± 0.3% out of 99.8% of the scale. Conversion time is 4.7 μs for 1024 channels.

MCA

After being digitalized by the ADC, the measurements are sent to a Multi-Channel Analyzer to store the spectrum. For this work it was used a memory buffer **SILENA 7329** with 4096 channels able to manage four spectrometers. Every channel corresponds to a certain time interval, so that the *n-th* channel contains the annihilation events occurred between *nT* and *(n+1)T*. Therefore, the total number of counts stored in every channel is equal to the number of pulses generated by the TAC in that time range. What's left, in order to achieve a correct deconvolution of the spectrum, is to evaluate the time resolution of the spectrometer and the channel-time conversion related to the MCA, i.e. the time interval *T* corresponding to a single channel.

The spectrometer calibration serves precisely this purpose. Through the procedure here described it can be determined the time interval corresponding to a single channel. To this purpose, a ^{60}Co is used. The lifetime spectrum produced by its nuclear decay, should be given by a delta function. Indeed, the source emits two gamma rays with similar energies (1.17 and 1.33 MeV) within 0.7 ps and they can be considered simultaneous in comparison with our time scale of several ns. However, but because of system non-idealities, it will result in a broadened function, called *resolution function*. As previously mentioned, stop signals are always delayed with respect to the start ones, so even though two signals arrive simultaneously, the relative spectrum is not placed at the first channel, but it is situated around the channel corresponding to the fixed delay. If it is introduced an additional delay, arbitrary chosen, it is found the same spectrum but shifted by a certain amount of channels corresponding to the delay. The same happens if more arbitrary delay are applied. Then the centroid of each curve is calculated using the weighted average formula:

$$x = \frac{\sum_{ch_1}^{ch_n} ch \cdot count(ch)}{\sum_{ch_1}^{ch_n} count(ch)}$$

(2.9)

where *ch* is the channel number and *count(ch)* is the number of counts at a certain channel. Once the values of the centroids for each curve are found, they are plotted versus the relative delay obtaining a straight fitting line whose angular coefficient represents the time interval per channel. For the apparatus employed in this work it was found a value of 10 ps/ch.

As it was stated, the spectrometer is characterized by a resolution function *R(t)*, that represents the system response to two simultaneous signals. But because of many sources of uncertainties, it cannot be a delta-like function. Knowing this function leads to a correct estimation of the time resolution of the apparatus, that is essential for the analysis of lifetime data. The spectrum obtained is the convolution between the physical spectrum and the system pulse response. Thus, the *R(t)* function is needed in order to perform an accurate deconvolution of the spectrum. The real broadened resolution function is responsible for smearing effects on the initial channels. Thus, the most perceivable effect is close to the origin, while time resolution effects are not so important for long lifetimes and this is favorable to our experiments since they concern the o-Ps lifetime that is the longest component of the deconvoluted spectrum. A good spectrometer is characterized by a symmetric pulse response *R(t)*, which is often approximated by a Gaussian curve, whose *full width at half maximum (FWHM)* is conventionally assumed to be the apparatus resolution.

The resolution function can be determined in practice exploiting again the decay of ^{60}Co. This radioisotope decays towards an excited state of ^{60}Ni which de-excite emitting two photon of 1.17 MeV and 1.33 MeV respectively. Since the second emission follows the first one only about 0.7 ps later, they can be considered to be emitted at the same time, indeed, the time span between them is insignificant compared to the measurements involved. The *FWHM* of this emission spectrum, as anticipated, is a figure of merit of the time resolutions. The aim is to try to have the lowest value possible through electronic device optimization.

The measures were carried out in two different electronic apparatuses in order to double the statistics. Thus, two lifetime spectrometers were used (out of the four allowed

by the memory buffer) and so four CFDs were needed (two start-stop couples). Before initiating the measures of interest, all the possible permutation for the CFDs at disposal were tried (with the only limit that the CFDs with only one boundary had to be used for the start channel), in order to find the best two start-stop couples to reach, not only the lowest *FWHM* possible, but also a similar value between them, to have comparable results. In the end the best compromise was to end up with the two couples returning values of *FWHM* of about 35 channels that with the channel-time conversion of 10 ps found previously, correspond approximately to 350 ps.

The estimation of the resolution obtainable by means of ^{60}Co is intrinsically inaccurate. In fact, if the 1.17 MeV photon approximates very well the start photon (1.274 MeV), the same cannot be said about the 1.33 MeV photon, that is very far from stop photon energy of 0.511 MeV, so it is considered as stop photon, a high energy photon degraded. Therefore, stop photon acquisition efficiency is lower than if the source was ^{22}Na (the radioisotope used in the experiments), and so the resolution function is worse. This resolution curve is larger than real curve, but this one is physically unobtainable since there isn't in nature a radionuclide which decays emitting simultaneously two photons of energy 1.274 MeV and 0.511 MeV. Making a rough estimate it can be said approximately that the real *FWHM* is about 10% lower than *FWHM* found with ^{60}Co source.

Cryostat and ITC

The aim of this work is to study the free volume in function of temperature. Thus, a cryostat must be employed which allows to reach temperatures until about 80K, that is the liquid nitrogen temperature, and up about 500K through a series of resistances. The cryogenic system used for this work is made up of different parts. The terminal part is a cylinder made of copper, material chosen for its high conductivity, so that it reaches in the least time possible the temperature set by the control system. In contact with the copper cylinder, on its upper side, there is a component called "room", in which are present all the resistances needed for heating. The cylinder is in contact with the "room", physically separated by a copper sheet above which tiny droplet of nitrogen fall over, and,

as soon as they touch the walls of the "room", they evaporate decreasing the temperature by conduction. The copper sheet is needed to prevent liquid nitrogen from dropping into the cylinder. On top of the "room" there is a Dewar, a vacuum container needed to store the liquid nitrogen and to pour it drop by drop in the "room" below. Liquid Nitrogen is inside the internal wall of the Dewar at a temperature of 77K, far lower than the ambient one, thus, it must be thermally isolated from the outside as much as possible. As known, there are three ways of exchanging heat: conduction, convection or irradiation. Conduction is neglected since there is vacuum between the internal and the external wall. There is no convection either since liquid nitrogen is stationary in the container. Finally, irradiation can be strongly reduced by adopting reflecting walls. The container cannot be hermetically sealed because nitrogen tends to evaporate and as a result there would be an accumulation of gaseous nitrogen that could lead to a dangerous increase of pressure, so the Dewar comes with an evacuation circuit connected with the external environment in order to expel any potentially dangerous excess of gas. In the terminal part of the container there is a capillary tube crossed by the stored liquid nitrogen whose diameter is controlled by a valve. The larger the diameter is, the more liquid nitrogen gets through, the faster will be the cooling. Once the "room" is cooled up, the copper cylinder and the polymer sample inside of it, get cooled too by conduction, reaching the desired temperature. Both the "room" and the copper cylinder are covered with a steel jacket and again vacuum is made in the middle, in order to avoid, here too, the thermal exchange with the exterior. But this steel jacket is a source of losses, it increases the distance between the scintillator and the source, thus the amount of photons impinging on the scintillator decreases because the solid angle relative to the scintillator is smaller.

Vacuum is obtained by means of two pumps. The first one is a rotary pump able to reach pressures of about 10^{-2} Pa, the second one is a turbo-molecular pump that start working from the vacuum created by the first one and goes up to 10^{-5} Pa. Pumps are kept working for a whole day to obtain an optimal vacuum, and this operation is repeated each time there is the need to change the sample in the copper cylinder.

In the "room" there is a resistance thermometer in order to update continuously the value of the temperature. An external Intelligent Temperature Controller unit is in charge to maintain the desired temperature, by varying the electrical current flowing into the resistances and the amount of liquid nitrogen reaching the "room" through the valve. Once reached the desired value, the system continues to deliver liquid nitrogen and at the same time it feds current to the resistances, eventually reaching a dynamic thermal equilibrium.

The cryostat used was the **DN 1714 Oxford** Instruments apparatus, purposely modified, while the temperature control unit used was the **Oxford ITC 4**.

HyperTerminal

Finally, the MCA can communicate with a computer through its serial port, in this way the acquired data can be transferred and stored on the machine in order to be studied afterward. The MCA and the computer must be able to talk one another, so it is needed a program that allows the PC to interface with the memory buffer. The program used for the data acquisition for this work purposes is HyperTerminal. This is an emulation program that supports text-based communication and it is capable of connecting to systems through the internet via Telnet or SSH, by Dial-Up Modem, or directly connected by a **RS232 serial cable** and **COM port** (this is the case). This terminal emulator is designed to mimic different types of terminal systems in order to communicate with any kind of external device by properly setting key parameters. The parameters to be initially chosen are the baud rate, data bits, parity, and flow control. First of all, the communication parameters have to be set on the MCA, then the commands on HyperTerminal come accordingly since they have to match the instructions of the buffer. The parameter adopted for this study are a baud rate of 9600 bits per second, a character length of 7 data bits, no parity, 1 for the stop bits and a hardware flow control. Then in the ASCII setup window all the checkboxes must be selected in order to allow a proper data exchange. After that the program has to be put in transfer mode so that is ready to receive the information. On the MCA the measures have to be stopped both on the first

and the second task (as stated before, two measures are performed at the same time and it possible to switch from one to another using the control panel of the memory buffer). Once the measurements are stopped, it is possible to select the copy option, and if the HyperTerminal was correctly configured and set ready to capture data, it immediately shows the information being transferred. It returns, in the end, two text files, one per task, where are reported all the numbers of the counts per channel. The 4096 channels are acquired divided in eight columns, thus subsequent manipulations are needed to unroll the data and study the full spectrum.

Chapter 3

Data processing

LT_polymer program

The analysis of the components of the spectrum is carried out using an appropriate program that is the LT Program, the specific version for polymers, by *Jerzy Kansy*. It takes as input the text file coming from the HyperTerminal Program, that contains all the information of the spectrum to be analyzed. It must first be modified into a layout readable by the LT Program, after that the user is required to enter a series of parameters that can be set free or be fixed to a specific value. These parameters concern the positron source, the transfer function *R(t)*, the number of components chosen, the background and others. Of course, the program operates on the free parameters in order to get the best fit between the hypothesized model and the experimental data, while the fixed parameters do not change during the research of the best approximation. The optimization proceeds through a nonlinear least-squares fitting, after the deconvolution of the experimental data. Hereinafter, the parameters chosen for this study are described in detail.

The first thing required are the initial and final channel among which the analysis should be performed. As left limit, it is chosen a channel on the left of the one considered as *zero*. It is chosen within a range of about a quarter of the *FWHM* of the *R(t)* that is about 10 channels. This choice is made in order to avoid information losses due to the effects of the convolution of the *R(t)* and the exponential components of the Gaussian (later it will be seen that these components are related with how the transfer function is represented by this program). For the right limit, it is simply chosen a channel where the spectrum starts to be horizontally flattened, i.e., the portion of the curve where are

accounted only the counts relating to the background noise, being careful to not include the final part of the longer exponential queue.

It is required the background. This value is already known with enough precision directly from the spectrum memorized in the MCA, it is simply the integral on the last channels (where the spectrum is flattened) divided by the number of channels chosen. Thus, this is a fixed parameter, and it is not modified during the iterations.

Information about the source are also required. Some positrons annihilate in the copper cylinder, generating a spurious signal that has to be filtered out during the deconvolution of the spectrum. In fact, the ^{22}Na source is hold in place between two foils of Kapton with a thickness of about 7 μm each. It is needed to specify the percentage of positrons that annihilate in the Kapton and their average life. From literature, in particular from the work by *Plotkowksi* [4], it is found that for the thickness of Kapton used in the experiments, it corresponds a fraction of positrons that annihilate in the support of 20% with an average lifetime of 386 ps. Since these values are known in advance, they are fixed parameters.

It is required the shape of the resolution function *R(t)*. Two possibilities are available. It can be chosen between a single Gaussian function with exponential queues:

$$R(t) = G(FWHM) \otimes e^{-t/\tau_l} \otimes e^{-t/\tau_r} \tag{3.1}$$

where $\otimes$ stand for the convolution operation, *G* represent the Gaussian function with a certain *Full Width at Half Maximum*, τ_l and τ_r are the time constants respectively of the left and right exponential queue. The second option consist in the sum of two or more Gaussians functions with different weights, *FWHM* and centroids:

$$R(t) = f_1 G(t, FWHM_1, \Delta_1) + f_2 G(t, FWHM_2, \Delta_2) + \dots \tag{3.2}$$

where *G(t,FWHM,Δ)* is the Gaussian, function of time, centered in Δ_i, with its *Full Width at Half Maximum FWHM_i* and f_i weight relative to the i-th term. In order to obtain accurate results, the single exponential-sided Gaussian turned out to be enough for this

work purposes. Moreover, as described previously, from ^{60}Co decay measurements it is known that the *FWHM* of the curve is about 350 ps. But this is not considered a fixed parameter during the fitting process since it is the result of an experimental measure, thus subjected to uncertainties and fluctuations, so it is only used as an initial guess from where the fitting can start. This value was fixed (not necessarily at 350 ps) only when an unrealistic fit was returned. The *time resolution* of the lifetime spectrometer affects much more the shorter lifetime component, the one of the *p-PS*, and luckily much less the higher *o-PS* lifetime which is the component of interest. Since the life of *p-PS* in vacuum is 125 ps and it undergoes to almost any changes passing from vacuum to matter, it was decided to fix the value of *FHWM* every time that, leaving it free, it was returned a lifetime under 100 ps, that could be reasonably considered as an unfeasible value. Fixing the value of the resolution worsen the fit since there is one degree of freedom less, but this worsening is acceptable because it is a compromise in order to obtain a realistic physical meaning (the aim is to obtain a description of the reality, not to obtain an artificially high χ^2).

It is finally required the number of components in which the spectrum has to be decomposed and if it the component has to be a discrete or a continuous variable. As discussed before, it was chosen to use three discrete components to deconvolute the spectrum. These lifetime parameters were set as free and, accordingly with the theoretical model, were chosen as initial guesses: 0.12 ns for the *p-PS* lifetime, 0.35 ns for the *free positrons* lifetime and 2 ns for the *o-PS* lifetime.

These analyses were carried on the spectra of five different samples for a preselected range of temperatures (from 230 K to 300 K). In this way the information embedded in the spectrum has been quantified. In fact, the program outputs are the lifetime values of the three components and their intensity. All the variables set initially as free, are shown with their statistical uncertainty. Furthermore, as already mentioned, a χ^2 test is given, that is useful to quantify the goodness of the fit. In addition to the numerical outputs, the results can be also displayed in graphical form, showing the experimental spectrum, the fitted spectrum, their difference (the residuals) and the three deconvoluted components.

Residuals are useful since the presence of systematic oscillations is the sign that the model is not satisfactory. An example is shown in the following figure.
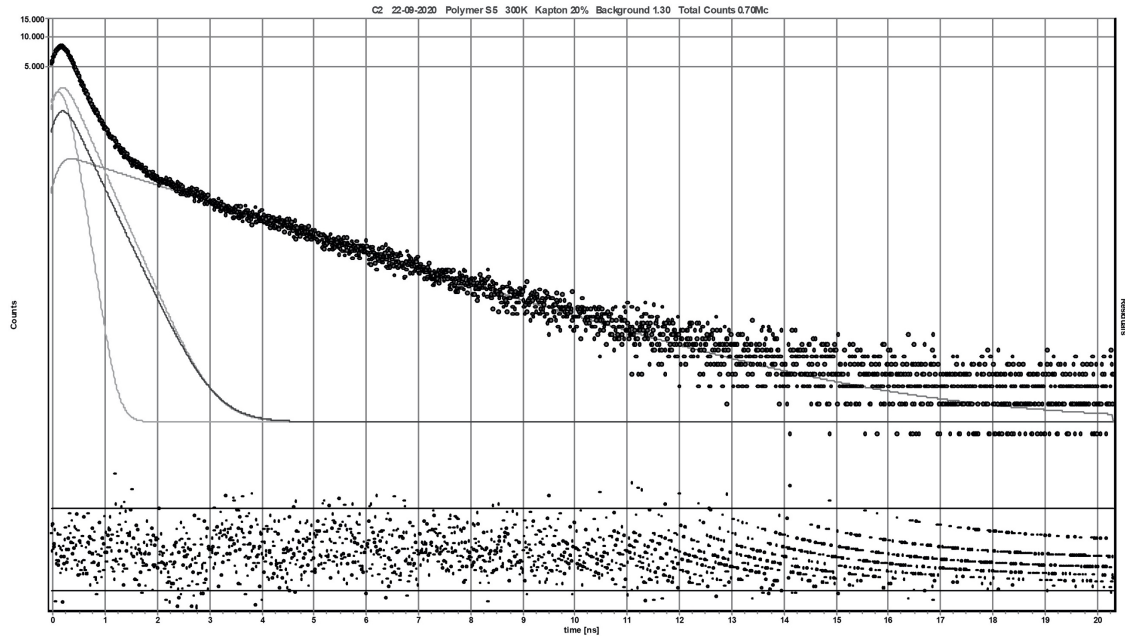

Figure 3.1 - Spectrum of a S5 polymer sample at 300K

On the x-axis is displayed the time frame in ns, obtained from the channel number through the channel-time conversion parameter calculated previously and resulting to be of 10 ps/ch. It can clearly be seen that there has been applied a cut-off around the 2000th channel (20 ns) and that it was chosen as start channel, one near to the centroid of the curve on the left side. On the y-axis is displayed the number of counts per channel that is clearly represented by the experimental dot-curve. While, of the four solid lines, three represent the discrete components in which the spectrum is deconvoluted and the fourth represent the positrons that annihilate in the Kapton.

In the end it was obtained a satisfactory statistical test, with a normalized χ^2 in the range 0.92-1.08 (very near to the ideal value of 1). It always has to be kept in mind that the results coming from the program were never taken as absolute truth, they were always checked (regardless of the χ^2 returned), asking if they would make sense in reality or not, following the criteria mentioned above.

Eventually these values were tabulated in function of the temperature focusing only on the *o-PS* lifetime, allowing the calculations described in the following paragraphs.

Table 2 - Average lifetime of o-Ps τ_3 in function of the temperature *T* for each elastomer

T [K]	230	240	250	260	270	280	290	300	310	315	320
S6	-	-	1.69	1.80	1.85	1.95	2.06	2.05	2.14	-	2.24
S5	-	-	2.38	2.41	2.46	2.50	2.55	2.58	2.60	-	2.64
S4	1.98	2.10	2.22	2.34	2.46	2.58	2.64	2.70	2.73	-	2.75
S3	2.08	2.18	2.26	2.36	2.46	2.55	2.64	2.69	-	2.71	-
S2	1.85	1.97	2.05	2.23	2.39	2.53	2.62	2.72	-	2.75	-

(row label: τ_3 [ns])
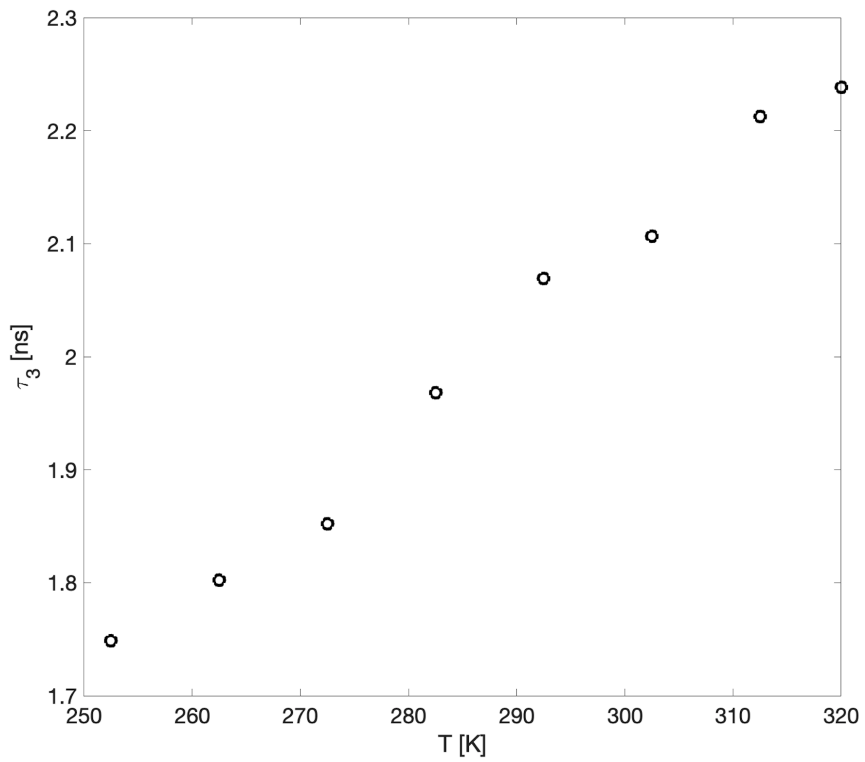
Figure 3.2 - o-Ps lifetime τ_3 as function of the temperature *T* for the polymer S6
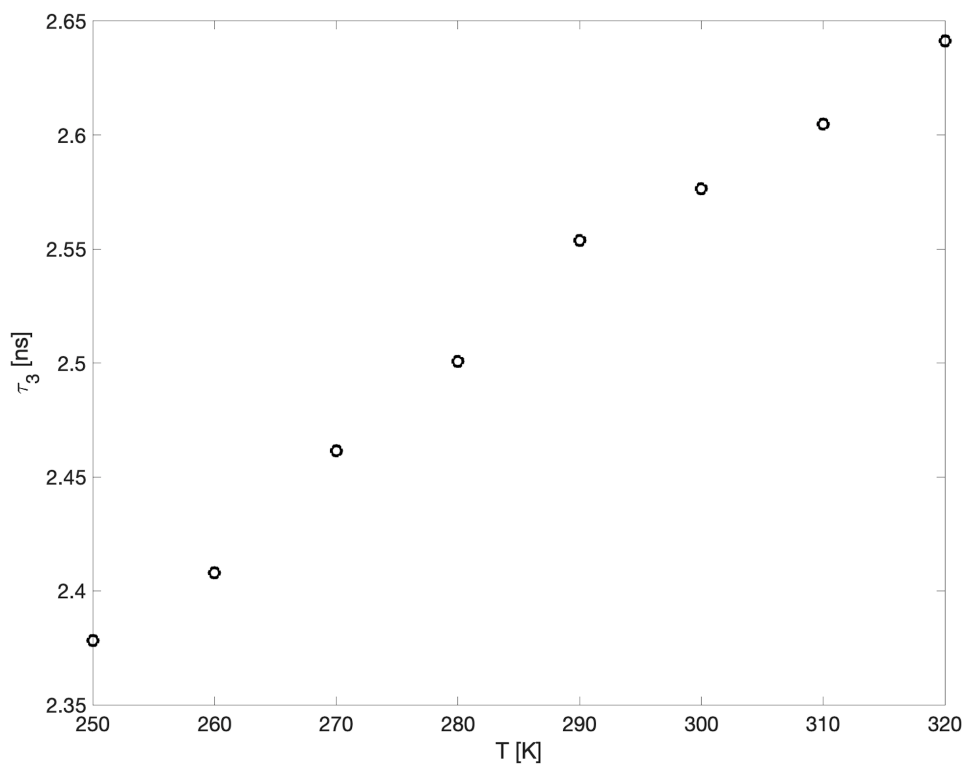
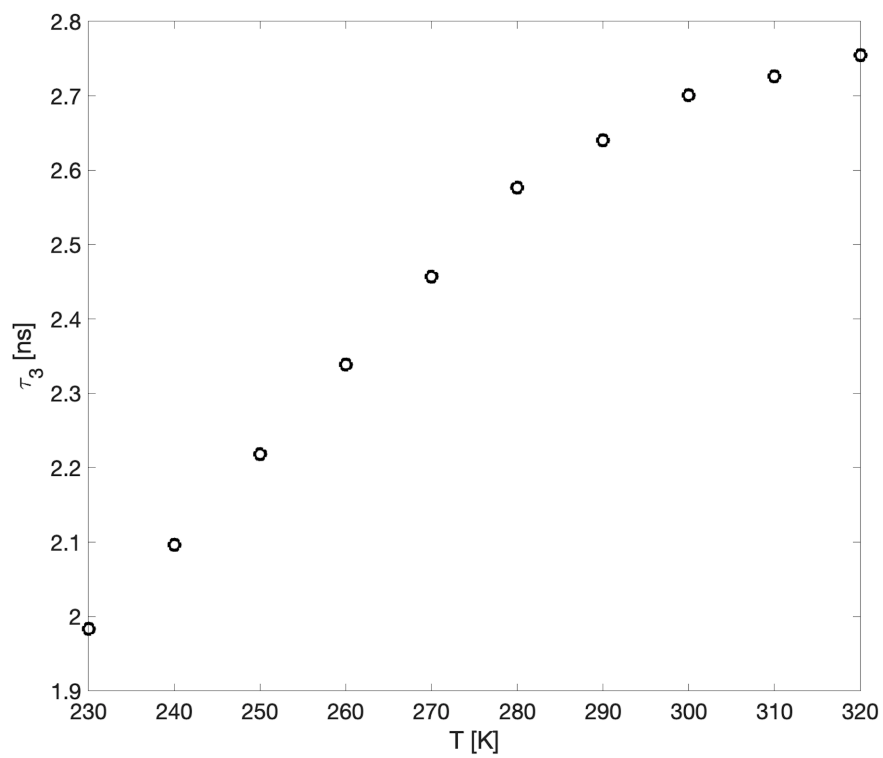**Figure 3.3** - *o-Ps* lifetime τ_3 as function of the temperature *T* for the polymer S5

Figure 3.4 - *o-Ps* lifetime τ_3 as function of the temperature *T* for the polymer S4
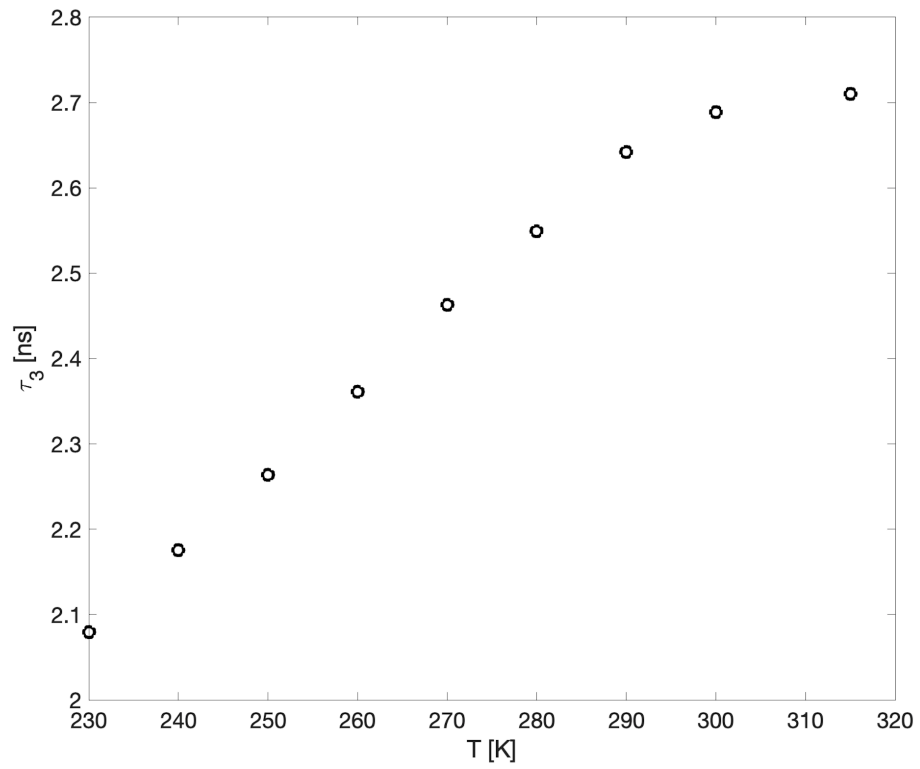
34

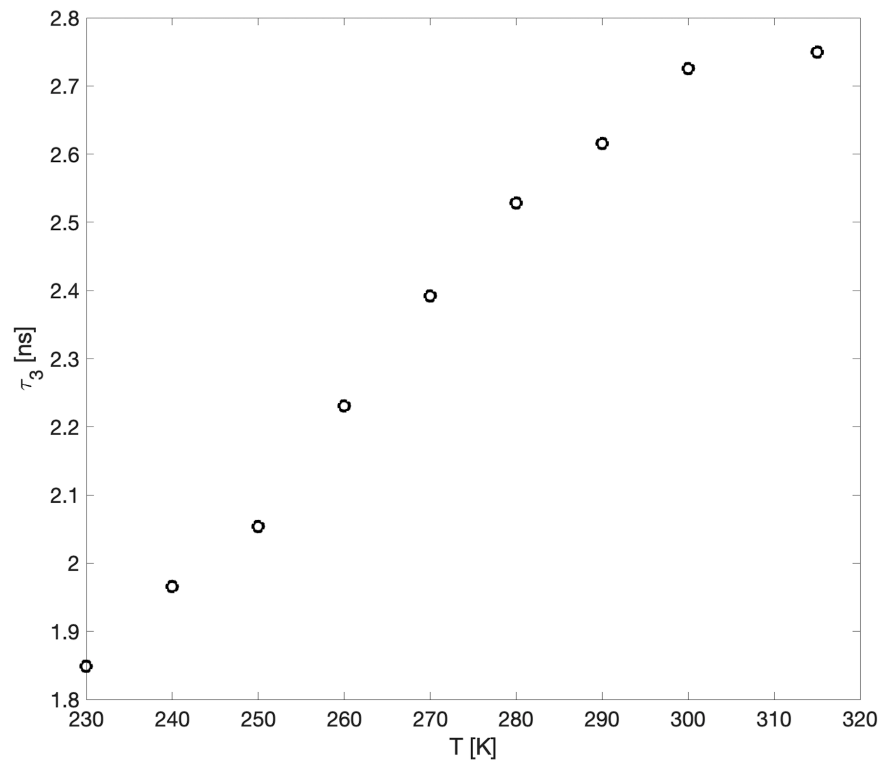**Figure 3.5** - *o-Ps* lifetime τ_3 as function of the temperature *T* for the polymer S3

Figure 3.6 - *o-Ps* lifetime τ_3 as function of the temperature *T* for the polymer S2

These graphics highlight a linear trend of the o-Ps lifetime with the temperature. But it is also noticeable that above around 300 K (depending on the polymer) there is a reduced increase of τ_3, it is a common feature for all the polymers studied. Many explanations were proposed in literature: formation of a Ps bubble [5], digging of holes by Ps itself [6] or a relaxation time of the molecular chains which is comparable to the Ps lifetime [7] . Whatever the explanation, in this temperature region it is safe to say that Ps cannot give reliable information on the free volume holes [8], therefore the discussion will be limited to temperatures below 300K. While for the lower limit it was chosen to not go below the glass transition temperature T_g of the polymer, since below this temperature inter- chains motions are strongly hindered, and the free volume shows only small variations with temperature (even if the relation continue to still be linear but with a lower slope). Furthermore, our results will be compared to the lattice-hole theory as explained later. Since this last is valid only for amorphous polymers at equilibrium, that is above the glass transition temperature, this is the only region of interest for the present study. Thus, the study was carried on the linear trend region between around 230K and 300K (again, each polymer needs specific choices). This region showed a correlation coefficient in the range 0.9946-0.9998 highlighting that the linear fit is a very good approximation (the ideal value would be 1).

Quantum mechanical models

The lifetimes of o-Ps have to be converted into the average size of the free volume holes v_h. To this purpose many mathematical models can be adopted in order to frame the Positronium in the cavity. The most popular one is the *Tao-Eldrup* model [9], [10]. The cavity hosting the Positronium is assumed to be a spherical void with radius *R*. In reality, such positronium trap would have a finite depth potential well, but in order to make calculation easier the depth is considered to be infinite and the radius is increased by a quantity *ΔR* evaluated empirically and set equal to 0.166 nm, introduced to take into account the penetration of the Ps wave function into the bulk. The electron density is supposed to be zero inside the sphere, so for *r < R*, and constant outside, so for *r > R*. The

relationship between the o-Ps lifetime τ_3 and the radius R is given by the following equation:

$$\lambda_p = \lambda_0 \left[\frac{\Delta R}{R + \Delta R} + \frac{1}{2\pi} \sin\left(2\pi \frac{R}{R + \Delta R} \right) \right]$$

(3.3)

where λ_p is the pickoff decay rate and λ_0, set equal to 2 ns^{-1}, is the annihilation rate of o-Ps in the presence of high electron density. While λ_p is directly related to the o-Ps lifetime. In fact, τ_3 is the inverse of the total decay rate λ_3, that is the sum of the pickoff decay rate and the intrinsic decay rate λ_i, equal to $1/142$ ns^{-1}:

$$\tau_3 = \frac{1}{\lambda_3} = \frac{1}{(\lambda_p + \lambda_i)}$$

(3.4)

Since the o-Ps lifetime is known from PALS analysis described above, λ_p can be easily calculated by reverting the **equation 3.4**. Thus, everything is known in the **equation 3.3** except for the radius R that is the desired value. This can be retrieved by using the *fzero function* in MATLAB in order to find the zeroes of the function. For the spherical geometry it is obtained a hole volume $v_h = (4/3)\pi R^3$. The volumes obtained are tabulated in function of the temperature as the o-Ps lifetimes from which they come from. As it will be shown in the next chapter, the spherical geometry hardly describes the reality in the investigated polymers, therefore other geometries must be adopted.

The second model adopted was a finite cylinder with radius R and height h. Where the height does not vary freely but it is linked to the radius by the aspect ratio q, so that it results $h = qR$. When q > 1 it is called elongated cylinder, while, when q < 1 it is called flattened cylinder. The relation between the o-Ps lifetime τ_3 and the radius R is in this case [11], [12]:

$$\lambda_p = \lambda_0(1 - P_1 P_2)$$

(3.5)

where:

$$P_1 = \frac{h}{h + \Delta h} + \frac{1}{\pi} sin \frac{\pi h}{h + \Delta h} \qquad (3.6)$$

$$P_2 = \frac{\int_0^{a_1 \frac{R}{R+\Delta R}} x J_0^2(x) dx}{\int_0^{a_1} x J_0^2(x) dx} \qquad (3.7)$$

where $J_0(x)$ is the zero-order Bessel function of the first kind and a_1 = 2.4048 is its first zero, while Δh is equal to 0.166 nm and again it is the quantity introduced to take in account the penetration of the Ps wave function into the bulk. In a similar way as before R is retrieved and the hole volume can be now calculated as $v_h = h\pi R^2 = q\pi R^3$. Again, the results are unsatisfactory so the investigation must proceed towards other models.

Since the same type of discrepancy has been obtained with both the previous geometries adopted, the reason of the deviation from the theory has been addressed to the assumption of isotropic expansion of the holes $v_h \propto R^3$. Dropping the isotropic assumption, a cylindrical geometry has again been considered to model the holes, the expansion along the direction of the radius R is supposed to be free, but this time the height h, that is still linked to the radius R by the aspect ratio q, grows slower than it as shown by the formula:

$$h = q R_0^{1-p} R^p \qquad (3.8)$$

where p is the anisotropy parameter, expected to be less than one (while for $p = 1$ we recover the previous isotropic expansion), and R_0 is the initial radius of the cylinder. Repeating the above steps, the radius R can be once again be retrieved and the hole volume calculated as $v_h = h\pi R^2 = q\pi R_0^{1-p} R^{2+p}$. This time, choosing suitable parameters q and p for each polymer, it is found a very good agreement between the theoretical and the experimental estimates of the free volume fraction, as it will be shown in the next chapter. But first, it has to be described, in the following paragraphs, how the experimental free volume fraction is obtained, and from where the theoretical one is derived, in order to finally confront them

Dilatometry

One thing still missing, in order to get the experimental free volume fraction, are the specific volumes V_s of the polymers. These data are also needed, together with the *Simha-Somcynsky* equation of state (explained in a specific chapter later), to evaluate the scaling parameters T^* and V^*, which in turn are needed to obtain the theoretical volume fraction. The data about the specific volumes are at our disposal from dilatometry studies [13]. Dilatometry measures the change in volume of a specimen subjected to different temperatures and pressures through a particular machine, the Pressure Volume Temperature (PVT) Apparatus. They are obtained and tabulated in function of the temperature, showing a linear trend. In the following tables are shown the specific volumes in function of the temperature for each polymer studied in this work [14].

Table 3 - Specific Volumes V_s as function of the temperature T for each elastomer

T [K]		343	333	323	313	303	296	293	283	273	263	258
V_s [cm³/g]	S6	1.0272	1.0208	1.0145	1.0083	1.0022	0.9980	0.0060	0.9906	0.9847	0.9790	0.9761
	S5	1.1386	1.1309	1.1234	1.1159	1.1085	1.1032	1.1010	1.0933	1.0860	1.0784	1.0748
	S4	1.1482	1.1407	1.1334	1.1259	1.1185	1.1134	1.1110	1.1035	1.0961	1.0894	1.0857
	S3	1.1428	1.1354	1.1280	1.1206	1.1132	1.1081	1.1058	1.0984	1.0911	1.0841	1.0805
	S2	1.1484	1.1408	1.1335	1.1261	1.1189	1.1138	1.1116	1.1042	1.0968	1.0894	1.0861

Experimental free volume fraction f

As it can be seen, the average volume of the cavities v_h and the specific volume V_s were evaluated at different temperatures. In order to use them to perform the following calculations, they are needed to be comparable (evaluated in the same conditions). As was stated before, they both showed a remarkable linear behavior, thus, without loss in accuracy they were both fitted with a linear interpolant and then their values were calculated for the same set of temperature chosen at the beginning of the study and that has been discussed above.

The total free volume is given by the sum of the specific hole free volume V_f and the interstitial free volume V_{if}. This last volume consists of local empty spaces, too minute to localize even the Ps. The specific hole free volume V_f can be expressed as the product of the number of holes per unit mass N times the average hole volume v_h: $V_f = Nv_h$. This free volume is accessible to Ps and it is the one calculated as the hole fraction in the lattice-hole theory (see next sub-chapter). Thus, this is the variable of interest for this work, while the interstitial free volume V_{fi} is associated with the occupied volume V_o. The specific volume V_s is then given by the sum of the specific free volume V_f and the occupied volume V_o:

$$V_s = V_f + V_o = Nv_h + V_o \qquad (3.9)$$

where the occupied volume V_o is now given by the sum of the Van der Waals volume and the interstitial free volume.

Indeed, the graphic showing the results of the specific volume V_s versus the average volume of the cavities v_h evaluated at the same temperatures (**Figures 3.7-3.21**), highlights a linear trend between the data, with a correlation coefficient higher than 0.99 for all the polymers. This was clearly expected, since both the variables showed a linear behavior with the temperature in the selected range of interest, that is, as explained before, above the glass transaction temperature and below the saturation temperature. N can be assumed constant, it is independent from the temperature, at least for $T > T_g$. Thus, these data can be fitted by straight lines. According to the **eq 3.9** N and V_o are

respectively the slope and the intercept of the linear fitting. Here below are shown the results. As it can be seen, whether it is used the spherical approximation, the isotropic cylindrical approximation or the anisotropic cylindrical one, the trend is always the same. A strongly linear behavior is highlighted, indeed all the results showed a correlation coefficient above 0.99.
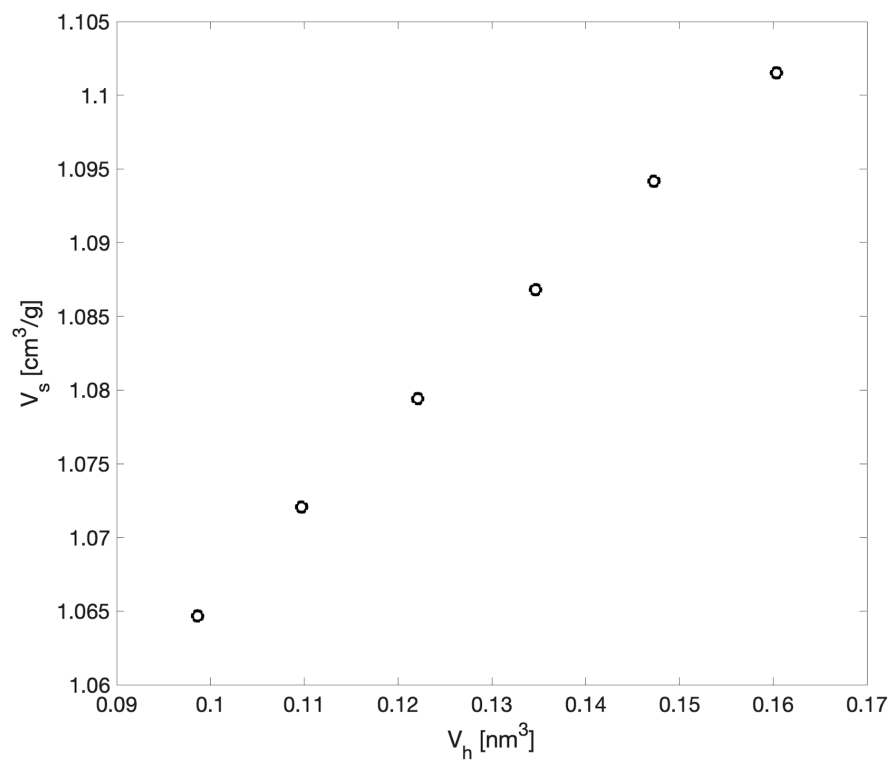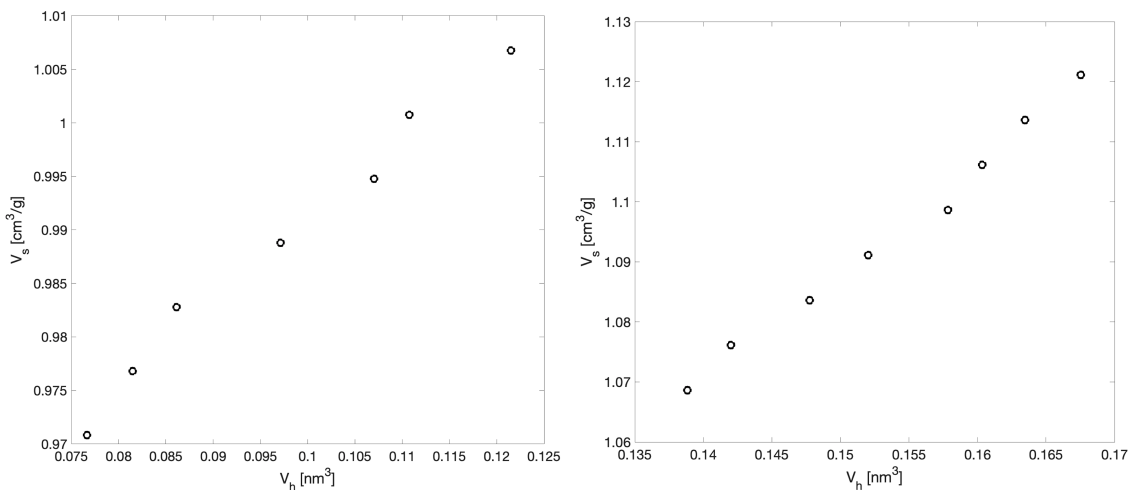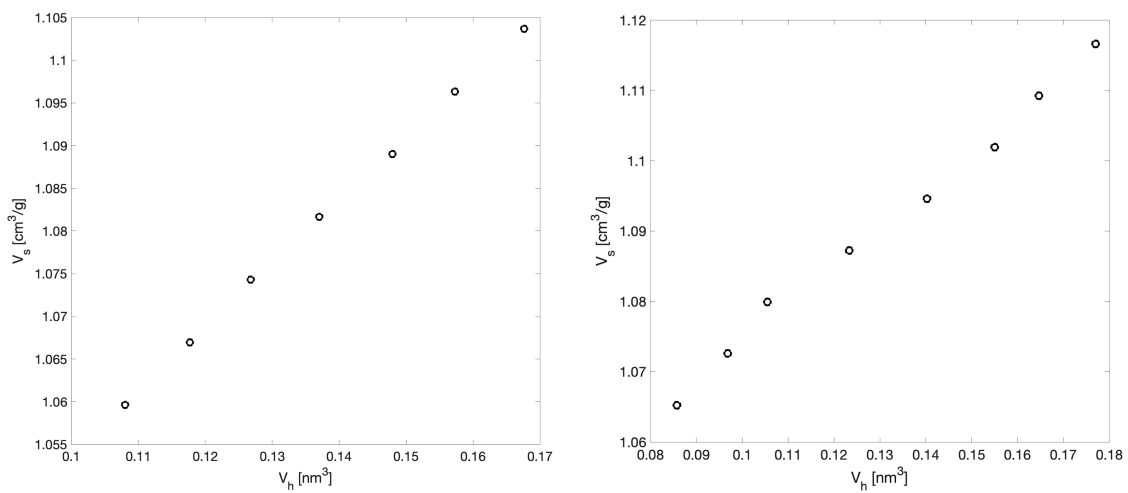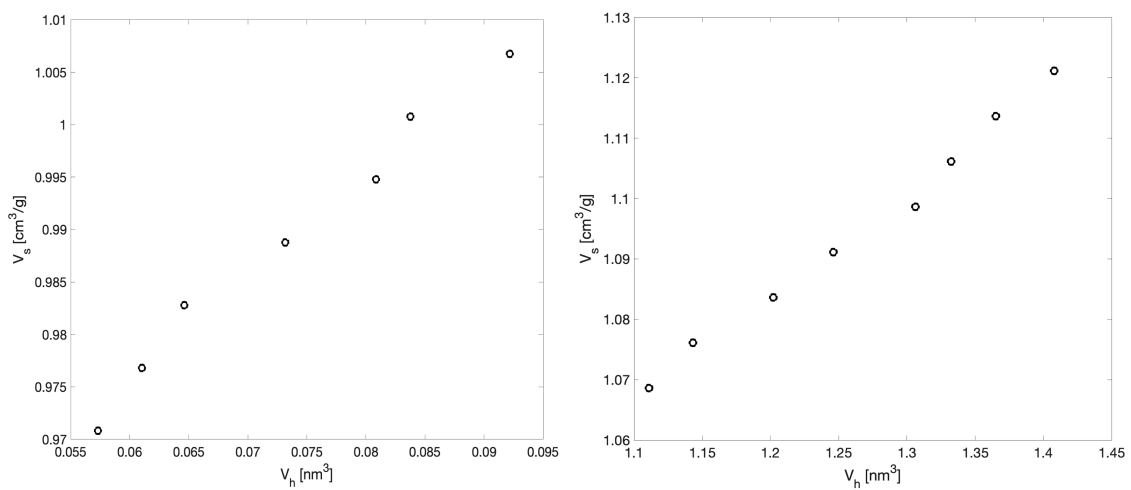

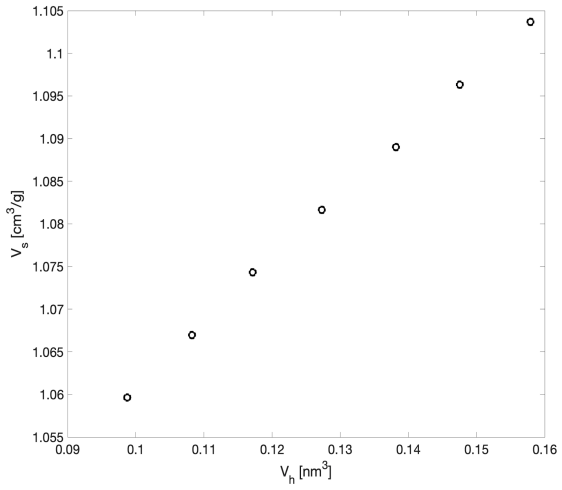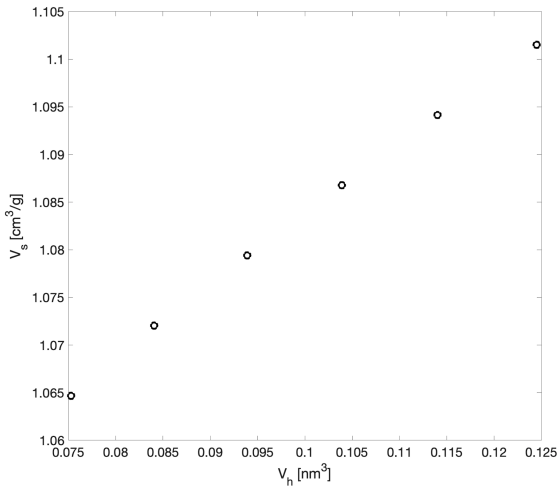Figure 3.7 - V_s in function of v_h in spherical approx. for the polymer S4

Figures 3.8, 3.9 - V_s in function of v_h in spherical approx. for polymers S5 and *S6*
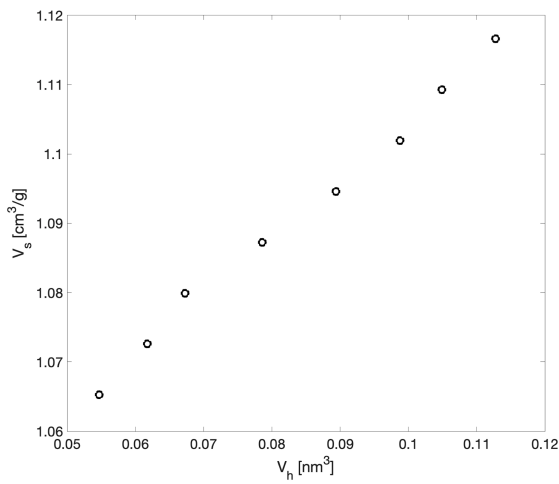

Figures 3.10, 3.11 - V_s in function of v_h in spherical approx. for polymers S*3* and *S2*
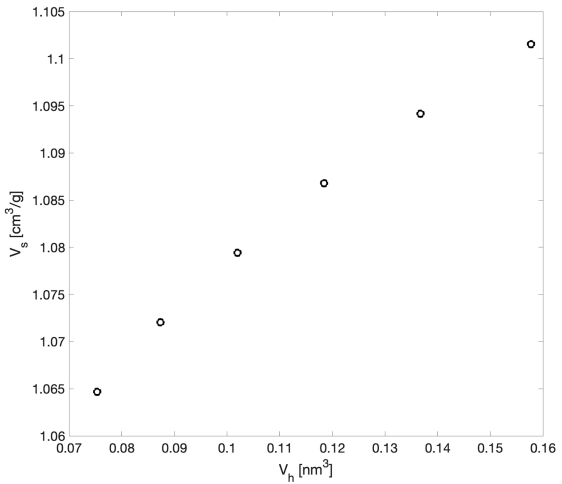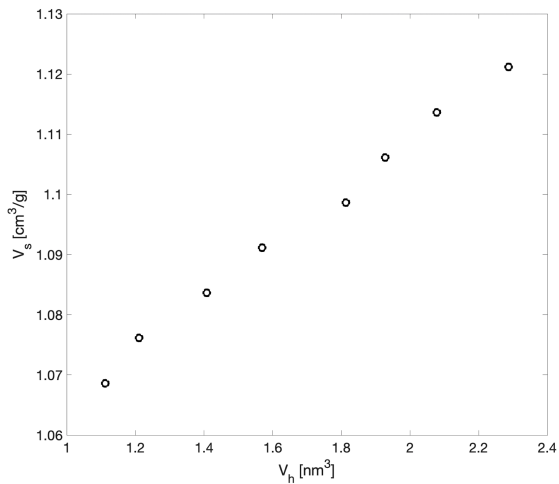

Figures 3.12, 3.13 - V_s in function of v_h in isotropic cylindrical approx. for polymers S*6* and *S5*
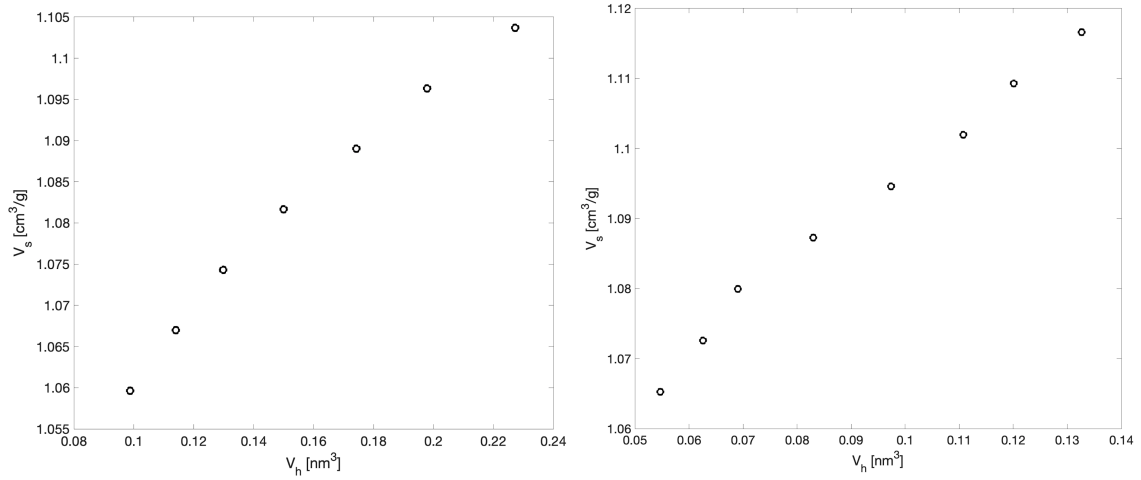
Figures 3.14, 3.15 - V_s in function of v_h in isotropic cylindrical approx. for polymers S*4* and *S3*
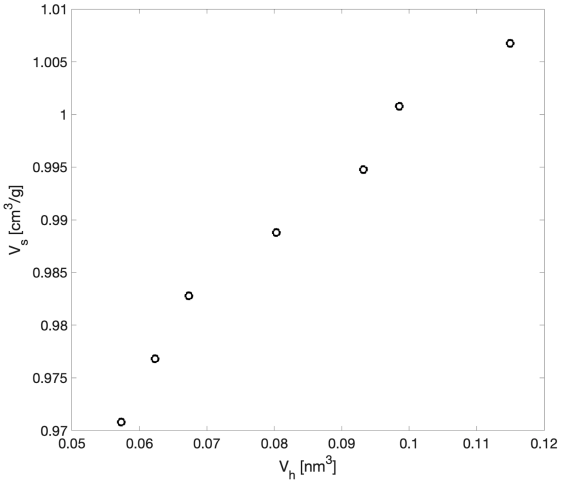
Figures 3.16, 3.17 - V_s in function of v_h in Isotropic cylindrical approx. for polymer S*2* and in anisotropic cylindrical approx. for polymer *S6*

Figures 3.18, 3.19 - V_s in function of v_h in anisotropic cylindrical approx. for polymers S*5* and *S4*

Figures 3.20, 3.21 - V_s in function of v_h in anisotropic cylindrical approx. for polymers S*3* and *S2*

Finally, now that *N* is available from the fitting of the previous graphs, and the free volume V_f is retrieved, the fractional free volume *f* can be evaluated according to the definition:

$$f = \frac{V_f}{V_s} = \frac{Nv_h}{Nv_h + V_o} \tag{3.10}$$

Its behavior versus the temperature will be compared with the one of the theoretical fractional free volume *h,* derived in the next chapter.

Theoretical free volume fraction *h*

One of the most popular theoretical models used to characterize the polymers consists in treating them as thermodynamic systems. The idea is to calculate the values of the missing thermodynamic coordinates starting from the physical known quantities solving an equation of state. From statistical mechanics a polymer can be approximated as a solid with a complex structure, in which the molecules are made up of long chains of monomers. According to this approximation, the material appears to be organized in a structure originated by the repetition of a single constituent, the cells. These cells can be occupied by the molecules of the polymer or can be empty. This model is so widespread because it allows to easily visualize the structure of the polymer and its molecular dynamics. To take in account that some cells are full and other empty, the occupied volume fraction *y* and the free volume fraction *h* are defined, linked by the relation *h = 1-y*. Using this model to describe the polymer, the theory of *Simha-Somcynsky* has come to outline an equation of state linking various thermodynamic quantities related to the polymer, moreover it establishes that the polymer, above the glass transition temperature T_g, can be seen as a thermodynamic system at equilibrium and so a second equation could be defined in order to describe it. The glass transition temperature T_g is a parameter characterizing amorphous polymers, it marks two different "regions" in which the polymer shows a totally different behavior. The kinetic behavior of the molecules is different, inter-chain motions are hindered, the so-called *cooperative motions* results not active under this temperature, and this translates at macroscopic level in different thermal properties, mechanical properties and many other properties. This is why from a thermodynamic point of view, a polymer above T_g can be seen as a thermodynamic equilibrium, while under T_g, the polymer is in a "frozen" condition, because of the slower movements of its chains, thus the hypothesis of equilibrium under these circumstances falls and it cannot be studied with the *Simha-Somcynsky* theory. This is why all the results shown previously were taken above the T_g, in order to correctly compare them with this theory. Under the hypothesis of the *Simha-Somcynsky* theory, a polymer can be

described by means of an equation in which appears four thermodynamic coordinates: the specific volume $\widetilde{V}$, the occupied volume fraction y, the temperature $\widetilde{T}$ and the pressure $\tilde{p}$. The general form of the *Simha-Somcynsky* equation is [3]:

$$\frac{\tilde{p}\widetilde{V}}{\widetilde{T}} = \left[1 - y(2^{\frac{1}{2}}y\widetilde{V})^{-\frac{1}{3}}\right]^{-1} + \frac{y}{\widetilde{T}}\left[2.002(y\widetilde{V})^{-4} - 2.409\left(y\widetilde{V}\right)^{-2}\right] \tag{3.11}$$

where $\tilde{p}$, $\widetilde{V}$, $\widetilde{T}$ are dimensionless parameters called reduced parameters and are defined as $\tilde{p} = p/p^*$, $\widetilde{T} = T/T^*$ and $\widetilde{V} = V/V^*$. While the quantities p^*, T^*, V^* are the scaling parameters, specific for each polymer. This form is useful because in this way the equation is valid for any amorphous polymer and the solution can be tabulated without having to solve each time the equation, the general results can be adapted to the specific polymer knowing its scaling parameters. The **eq 3.11** takes in account 4 variables, but in most cases the variables are reduced to three, since usually the results are derived in the most common case of atmospheric pressure, in these conditions the reduced parameter $\tilde{p}$ tends to zero and the equation can be rewritten as:

$$\widetilde{T} = 2y(y\widetilde{V})^{-2}\left[1.2045 - 1.011(y\widetilde{V})^{-2}\right]\left[1 - 2^{-\frac{1}{6}}y(y\widetilde{V})^{-\frac{1}{3}}\right] \tag{3.12}$$

Out of the three remaining variables, the specific volume and the occupied volume fraction are the unknowns, while the temperature is known and fixed each time. Thus, there are two unknowns and only one equation, it is needed another equation in order to get the specific volume and the occupied volume fraction values. For the assumptions stated before, the polymer above the T_g can be considered in thermodynamic equilibrium, this allows to write another equation related to the minimization of the free energy of the system [15], [16]:

$$1 + y^{-1}\ln(1-y) = \left[y(2^{\frac{1}{2}}y\widetilde{V})^{-\frac{1}{3}} - \frac{1}{3}\right]\left[1 - y(2^{\frac{1}{2}}y\widetilde{V})^{-\frac{1}{3}}\right]^{-1} + \frac{y}{6\widetilde{T}}\left[2.409(y\widetilde{V})^{-2} - 3.033(y\widetilde{V})^{-4}\right] \tag{3.13}$$

Solving these two combined equations leads to obtain the unknown values of y and $\widetilde{V}$. Now it can be better understood the need of considering the polymer at thermal

equilibrium, outside this hypothesis the **eq 3.13** is no longer valid and so the variables could not be calculated.

Once *y* is known, the free volume fraction *h* could be calculated through the formula *h = 1-y*. Thus, once the values of *V** and *T** are available, it is possible to obtain a theoretical estimation of *h* that can be compared with the experimental data to check their accuracy.

Finally, only *V** and *T** are missing to complete the analysis. They will be then put in relation with the general equation through the reduced parameters $\widetilde{T} = T/T^*$ and $\widetilde{V} = V/V^*$. The scaling parameters can be obtained starting from the experimental specific volumes V_s in function of the temperature *T* found with dilatometry. For amorphous polymers above T_g the following empirical relationship can be written [17], which is successfully used for a wide class of polymers [18]:

$$\ln\left(\frac{V_s}{V^*}\right) = A + B\left(\frac{T}{T^*}\right)^{\frac{3}{2}}$$

(3.14)

where *A* and *B* are universal constants whose values are *A = -0.1033* and *B = 23.835*. The **eq 3.14** can be rewritten in this equivalent form:

$$\ln(V_s) = \left[\frac{B}{T^{*\frac{3}{2}}}\right] T^{\frac{3}{2}} + [A + \ln(V^*)]$$

(3.15)

This equation is in the form *z = Cx+D* where *z = ln(V_s)*, *C = [B/T*^{3/2}]* and *D = [A+ln(V*)]* that simply represents the equation of a straight line. As was mentioned before, the specific volumes V_s in function of the temperature *T* are available from dilatometry for each polymer (see the inherent sub-chapter). From these values it is possible to obtain a graphic showing *z = ln(V)* in function of *x = T^{3/2}*. A linear fit of these data is done in order to obtain the experimental equation of the line *z = Cx+D*. The universal constants *A* and *B* are known, from the fit *C* and *D* are now also known, thus, *T** and *V** can be finally calculated and be used to adapt the general *Simha-Somcynsky* equation to the specific polymer.

Here below are shown two tables summing up the results of what were discussed in this chapter. Basically, in these tables there are all the necessary information from which the theoretical free volume fraction *h* can be derived [14], [19].

Table 4 - Scaling parameters values for each polymer.

Polymer	Fitting Line Equation	V* [cm³/g]	T* [K]
S6	y = 2.3080e-5*x - 0.1197	0,9839	10222
S5	y = 2.6105e-5*x - 0.0353	1,0705	9416
S4	y = 2.5432e-5*x - 0.0227	1,0841	9582
S3	y = 2.5446e-5*x - 0.0275	1,0789	9578
S2	y = 2.5314e-5*x - 0.0218	1,0851	9612

Table 5 - Theoretical free volume fraction *h* in function of the reduced temperature $\widetilde{T}$.

$\tilde{V}$	$\tilde{T} \times 10^2$	$(1-y) \times 10^2$	$y\tilde{V}$	$(dy/d\tilde{T})_l$
0.95	1.6531	0.2816	0.947324	
0.96	1.9115	1.0297	0.950115	3.6285
0.97	2.1206	1.9090	0.951483	4.5068
0.98	2.3105	2.8200	0.952364	4.9584
0.99	2.4891	3.7350	0.953023	5.2215
1.00	2.6598	4.6437	0.953563	5.3948
1.01	2.8240	5.5414	0.954032	5.5176
1.02	2.9828	6.4258	0.954457	5.6132
1.03	3.1366	7.2958	0.954853	5.6881
1.04	3.2861	8.1510	0.955229	5.7518
1.05	3.4314	8.9912	0.955592	5.8076
1.06	3.5729	9.8165	0.955945	5.8547
1.07	3.7108	10.6269	0.956292	5.8966
1.08	3.8453	11.4227	0.956634	5.9347
1.09	3.9766	12.2043	0.956974	5.9660
1.10	4.1049	12.9718	0.957311	6.0025
1.11	4.2301	13.7255	0.957647	6.0286
1.12	4.3526	14.4659	0.957982	6.0571
1.13	4.4724	15.1932	0.958317	
1.14	4.5896	15.9077	0.958652	
1.15	4.7043	16.6098	0.958988	
1.16	4.8166	17.2997	0.959324	
1.17	4.9266	17.9777	0.959661	
1.18	5.0343	18.6442	0.959999	
1.19	5.1399	19.2994	0.960338	
1.20	5.2435	19.9435	0.960677	
1.21	5.3450	20.5770	0.961018	
1.22	5.4445	21.2000	0.961360	
1.23	5.5422	21.8127	0.961704	
1.24	5.6380	22.4155	0.962048	
1.25	5.7320	23.0085	0.962394	
1.26	5.8243	23.5920	0.962741	
1.27	5.9150	24.1663	0.963089	
1.28	6.0040	24.7314	0.963438	
1.29	6.0914	25.2877	0.963788	
1.30	6.1773	25.8354	0.964140	
1.31	6.2617	26.3746	0.964493	
1.32	6.3447	26.9056	0.964846	
1.33	6.4262	27.4285	0.965202	
1.34	6.5064	27.9434	0.965558	
1.35	6.5852	28.4507	0.965915	
1.36	6.6626	28.9505	0.966274	
1.37	6.7389	29.4428	0.966633	

Chapter 4

Final results

Here it is shown the final comparison between the two experimental and theoretical free volume fractions. Starting from the results obtained by approximating the cavities as spheres. It can be seen that f found from experiments is systematically higher than h coming from the theoretical model.
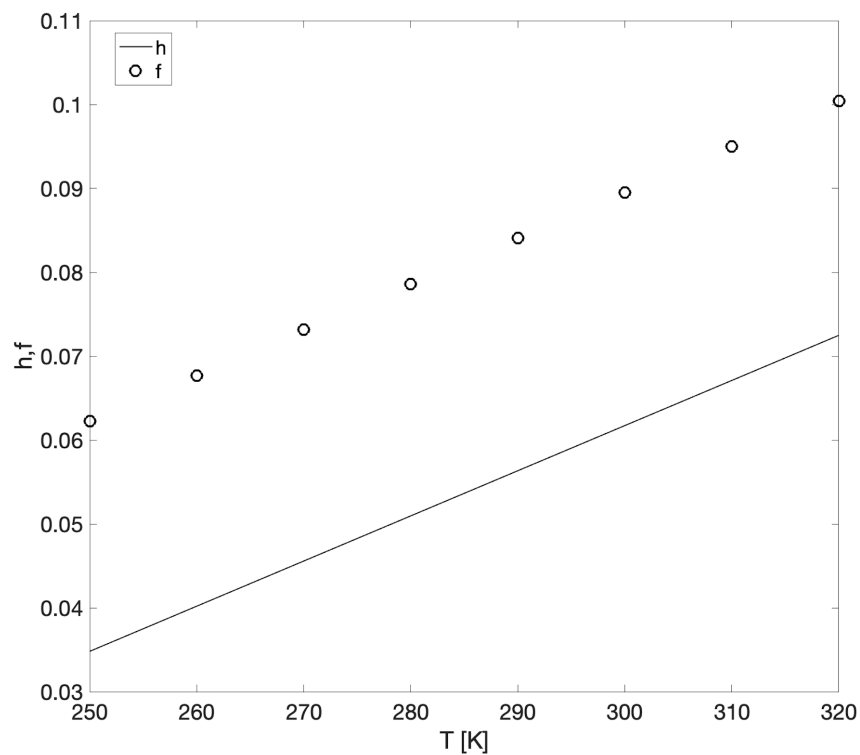

Figure 4.1 – Comparison between h, f in spherical approximation for the polymer S6
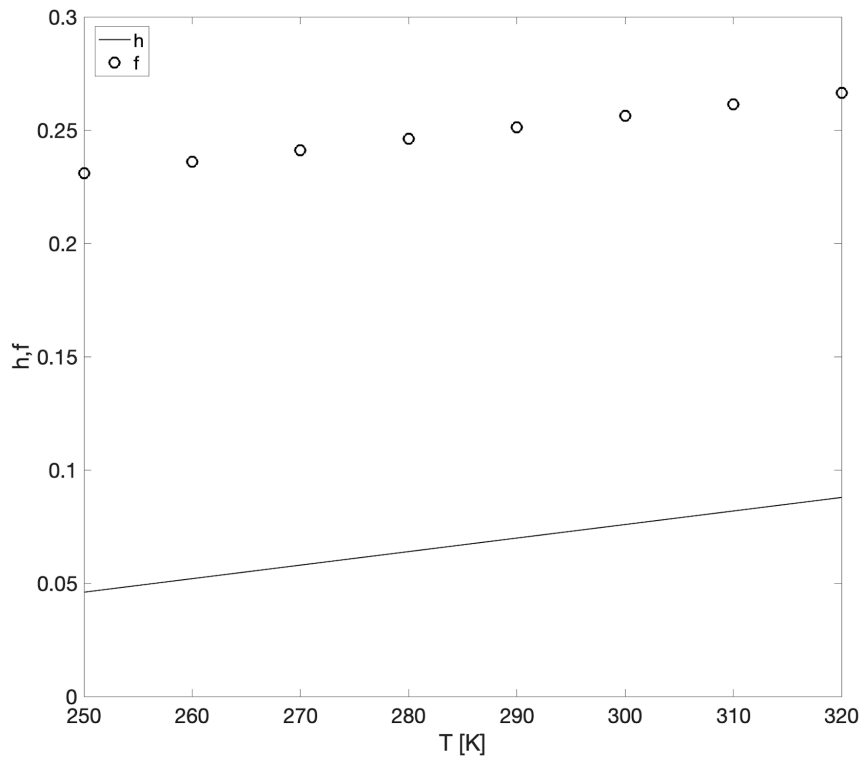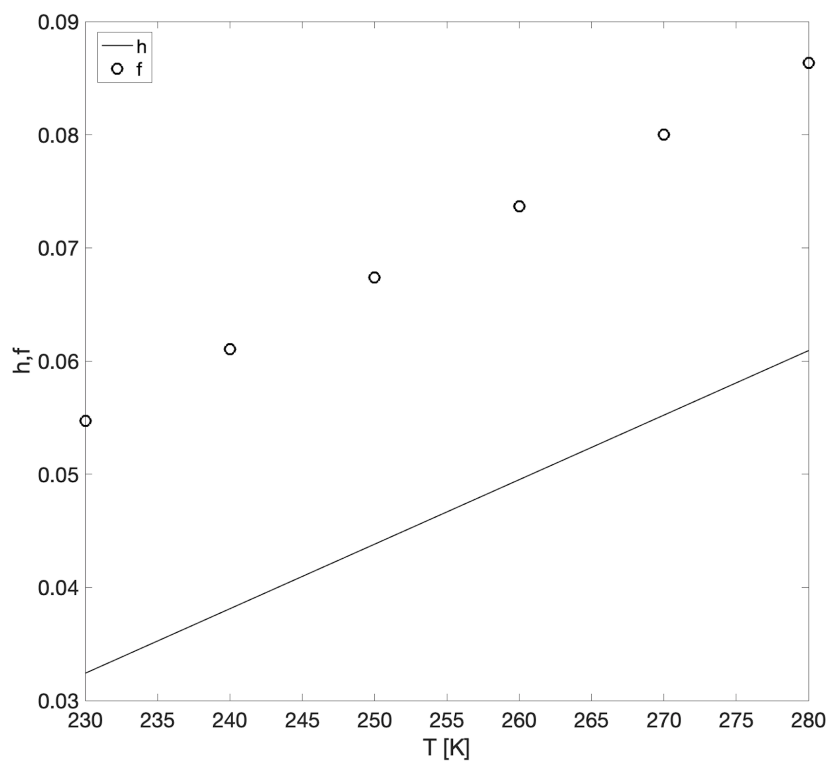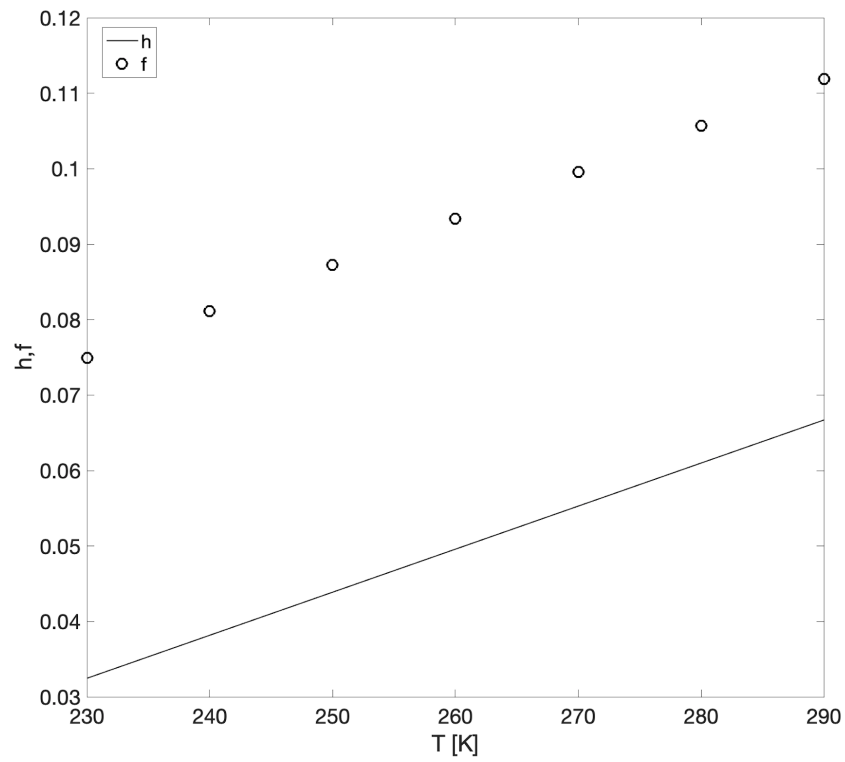
Figure 4.2 - Comparison between *h, f* in spherical approximation for the polymer S5

Figure 4.3 - Comparison between *h, f* in spherical approximation for the polymer S4

Figure 4.4 - Comparison between *h, f* in spherical approximation for the polymer S3
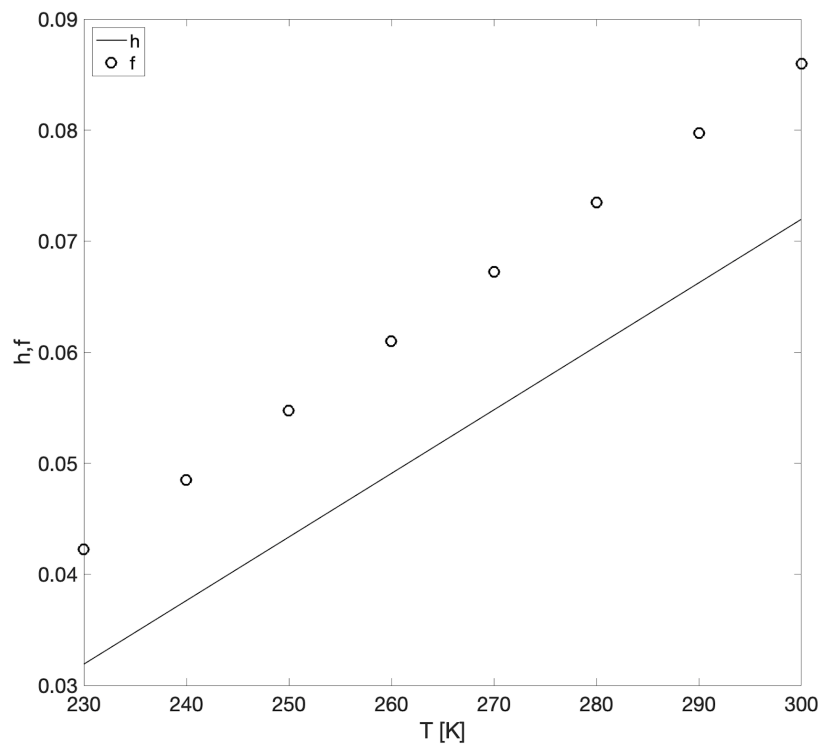
Figure 4.5 - Comparison between *h, f* in spherical approximation for the polymer S2

Here are shown the results obtained for the isotropic cylindrical approximation compared with the ones coming from the spherical approximation. A specific aspect ratio *q* was used for each polymer, trying to obtain the best fit. But it can be seen that the results are similar to the one obtained with the spherical approximation. This is a sign that an isotropic expansion for the cavities could not be a valid assumption.
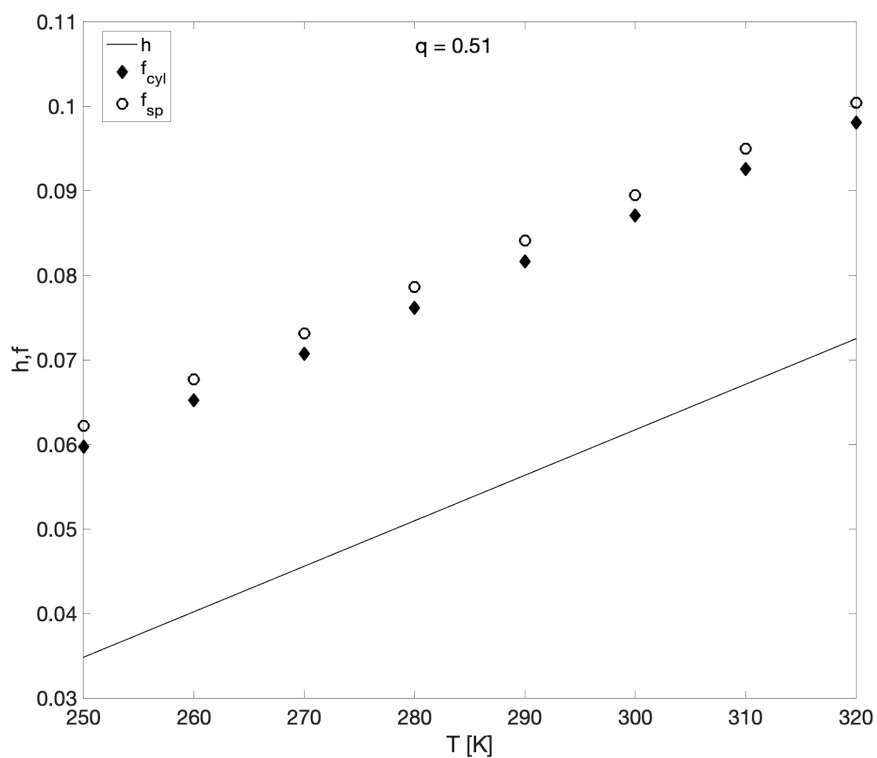
Figure 4.6 - Comparison between *h, f* in isotropic cylindrical approx. for the polymer S6
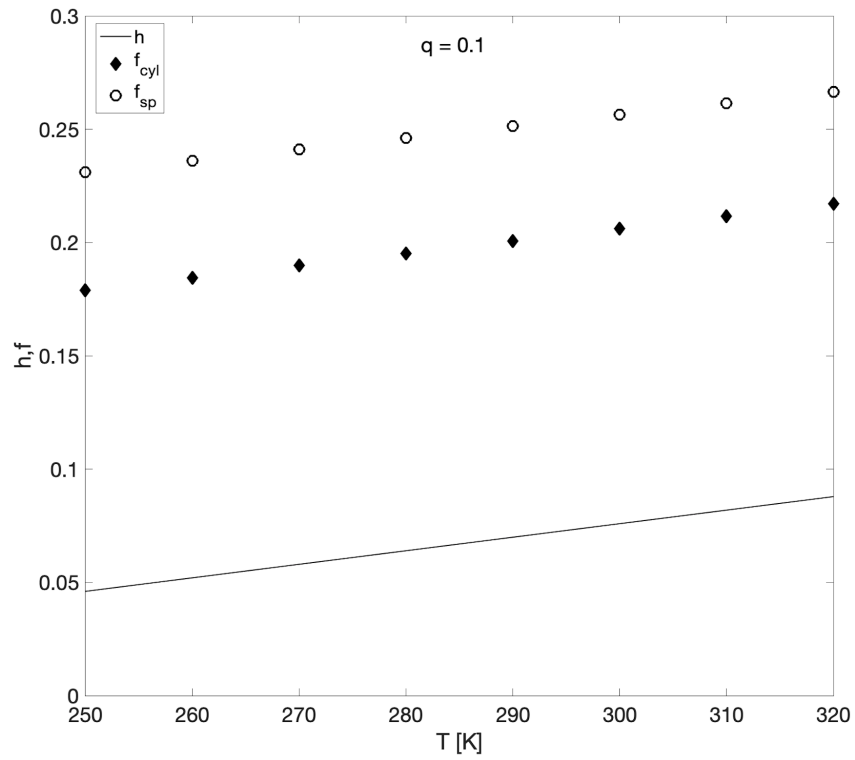
Figure 4.7 - Comparison between *h, f* in isotropic cylindrical approx. for the polymer S5
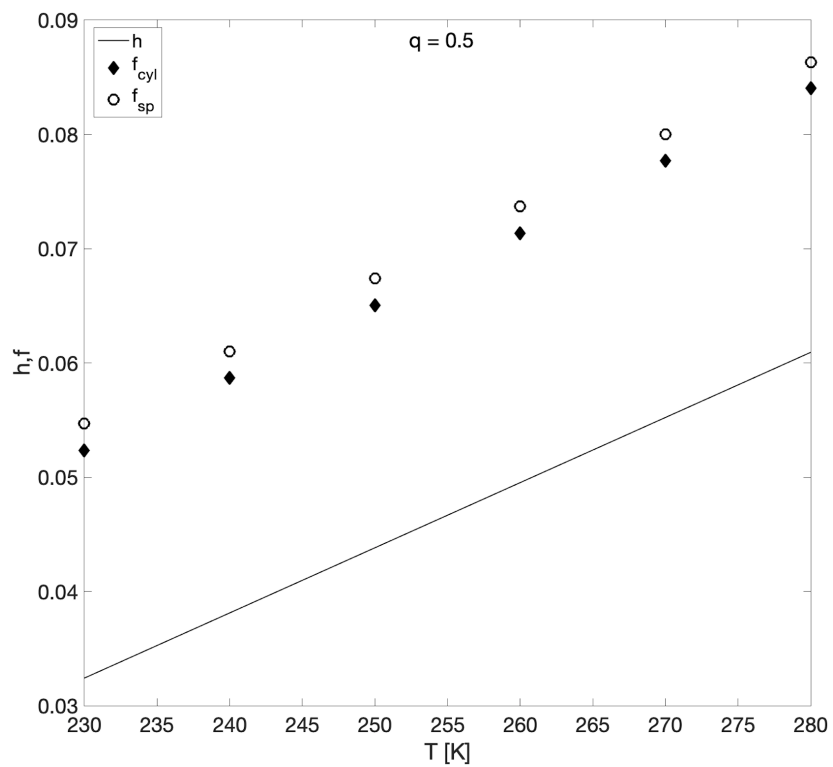
Figure 4.8 - Comparison between *h, f* in isotropic cylindrical approx. for the polymer S4
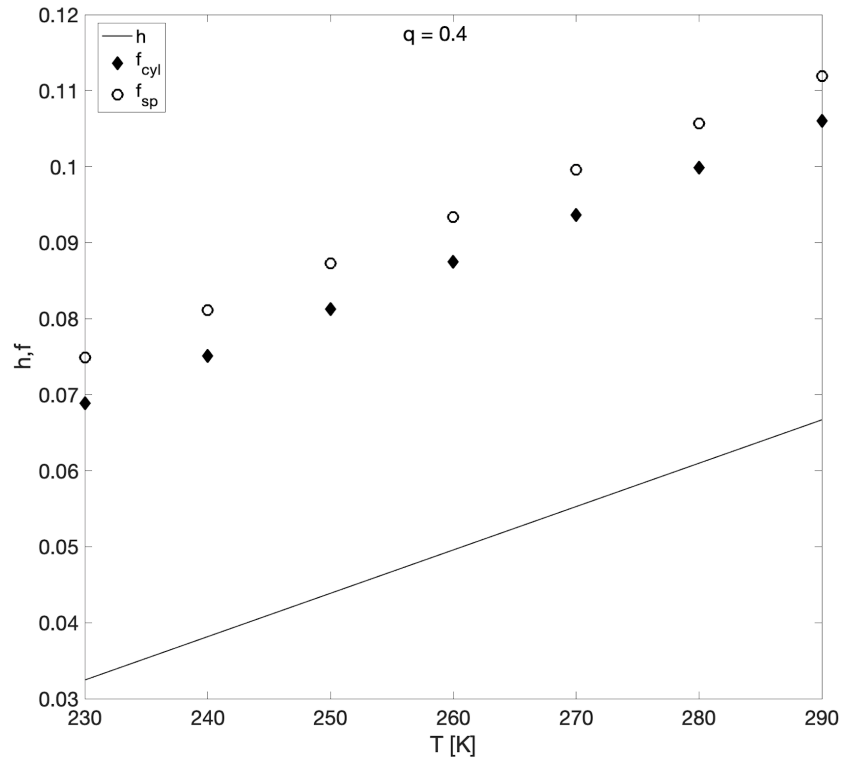
Figure 4.9 - Comparison between *h, f* in isotropic cylindrical approx. for the polymer S3
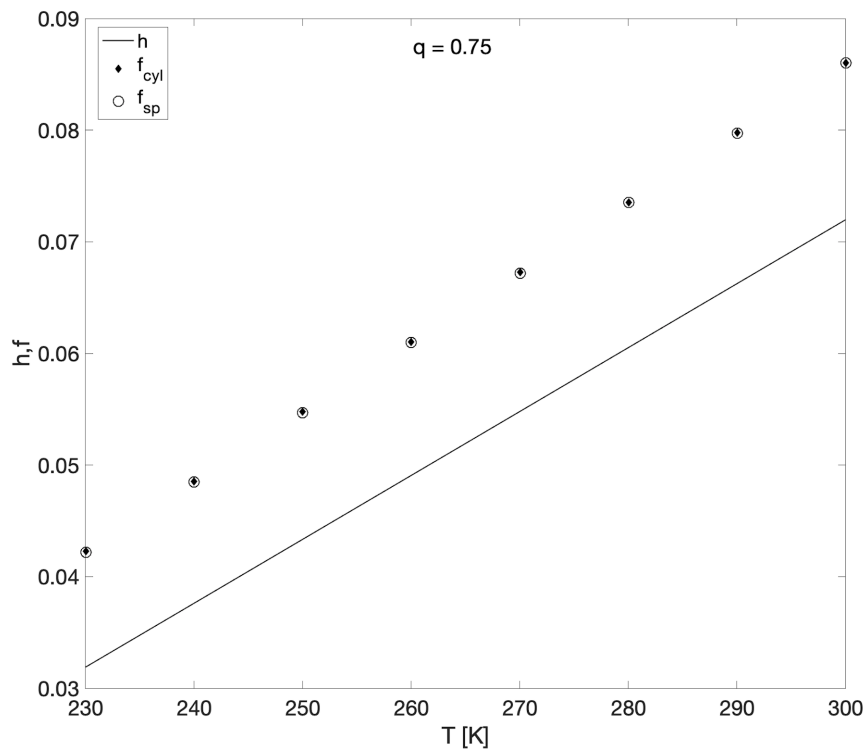

Figure 4.10 - Comparison between *h, f* in isotropic cylindrical approx. for the polymer S2

Finally, are shown the results for the anisotropic cylindrical approximation compared with the ones of the spherical approximation. As It can be seen, there is a very good agreement between the experimental free volume fraction f the theoretical free volume fraction h. Also in this case, an aspect ratio q, combined with an anisotropy parameter p, specifics for each polymer, were used in order to obtain the best fit.
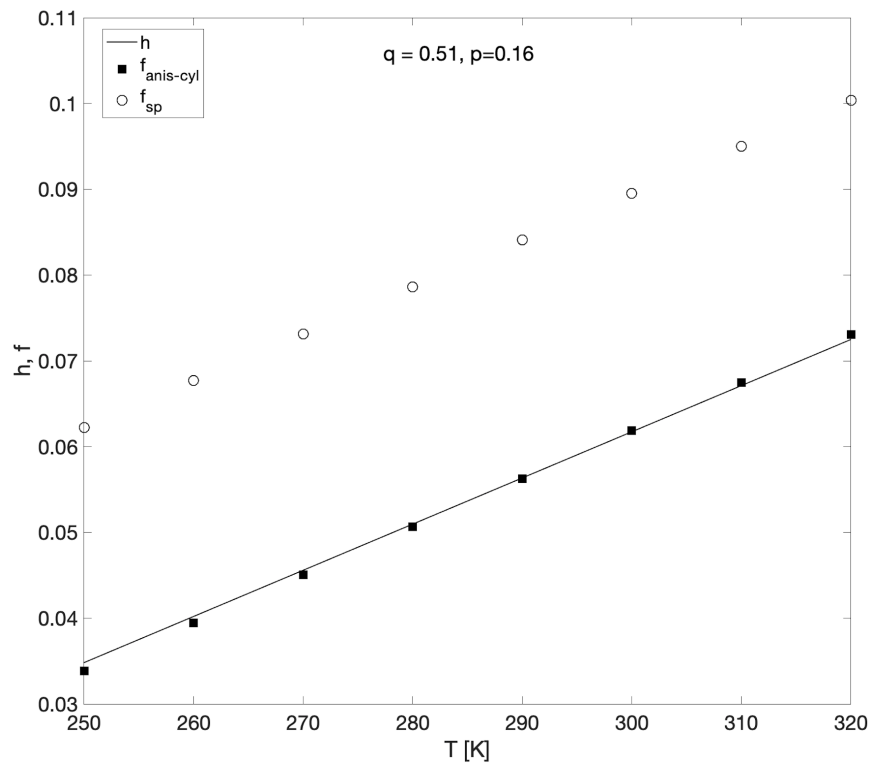

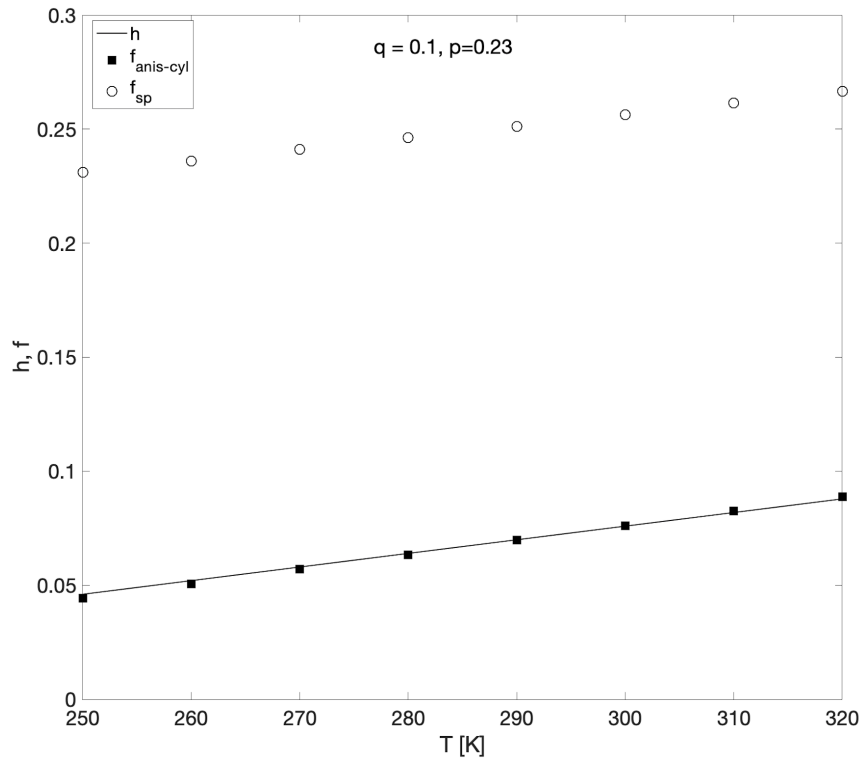Figure 4.11 - Comparison between h, f in anisotropic cylindrical approx. for the polymer S6

Figure 4.12 - Comparison between *h, f* in anisotropic cylindrical approx. for the polymer S5

Figure 4.13 - Comparison between *h, f* in anisotropic cylindrical approx. for the polymer S4

Figure 4.14 - Comparison between *h, f* in anisotropic cylindrical approx. for the polymer S3
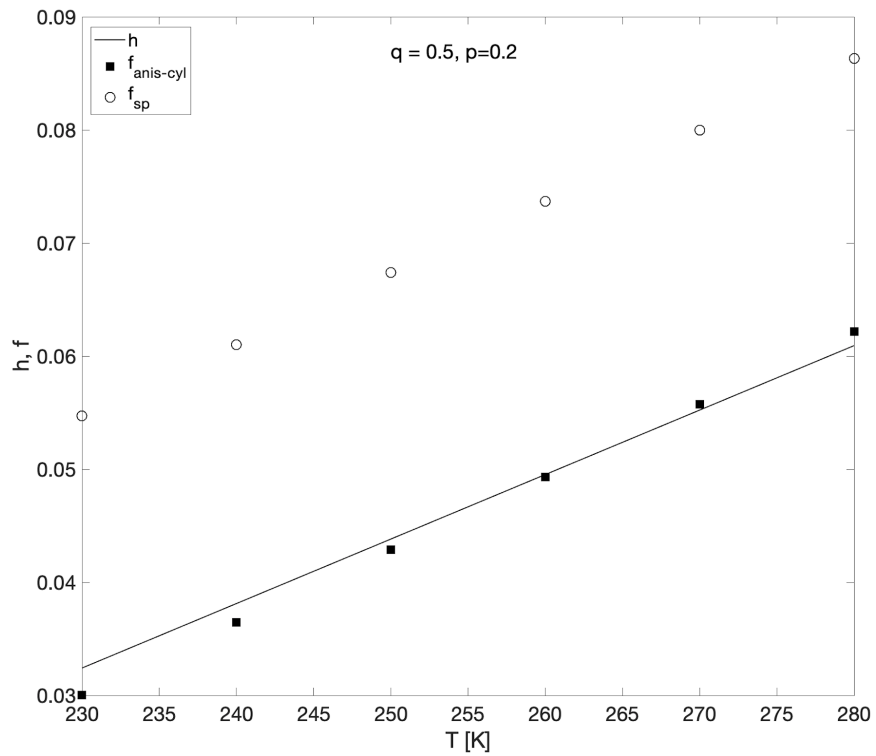

Figure 4.15 - Comparison between *h, f* in anisotropic cylindrical approx. for the polymer S2
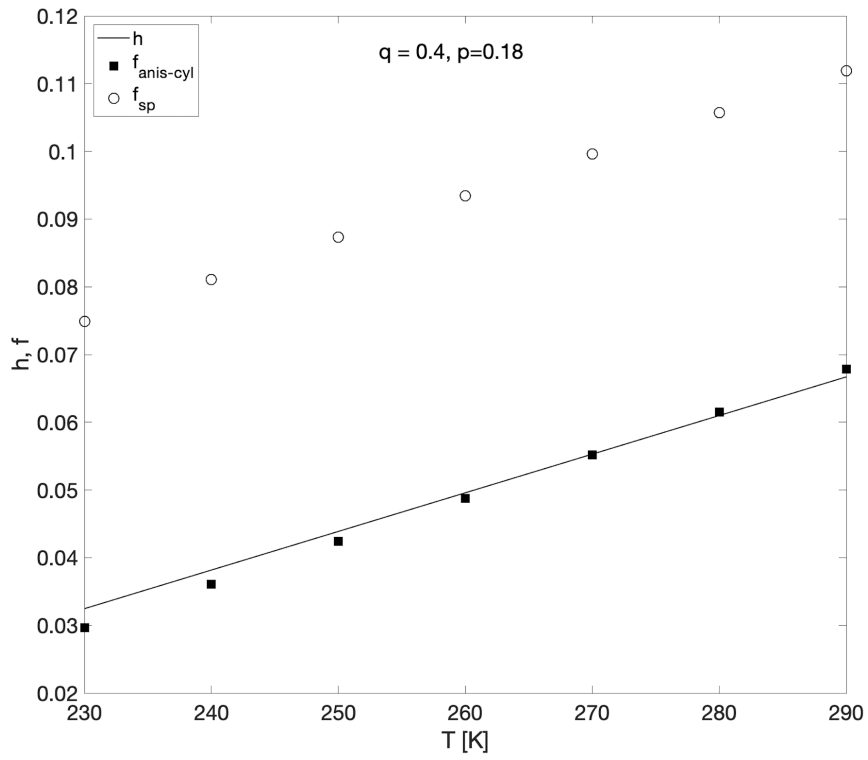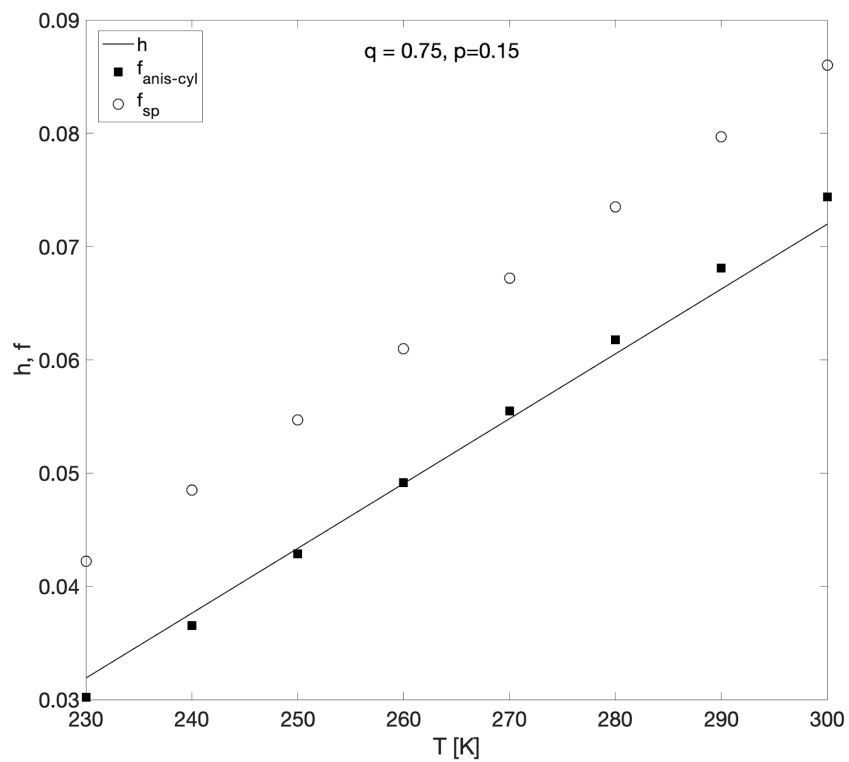
Chapter 5

Conclusions

In conclusion, PALS in combination with specific volume data coming from PVT measurements makes possible the determination of the free volume fraction of a polymer with respect of the temperature. The results depend on the geometry adopted for the holes, as well as on the expansion model chosen, isotropic or anisotropic. A comparison between PALS data and the predictions from the *Simha-Somcynsky* lattice-hole theory allows to gain insight into the hole structure by providing information about their morphology. Indeed, as seen in the final results, the anisotropic cylinder approximation gave a far better agreement with the theory than the other two geometries adopted. The best fit, for the elastomers under study, was given by a disk-like geometry expanding anisotropically. In particular, these results were obtained for cylinders with an aspect ratio $q < 1$ that is a flattened cylinder geometry, and an anisotropy parameter p around 0.2, meaning that the cylinder radius grow faster than its height (both parameters were different for each polymer but showed the same trend). This does not mean that the spherical geometry necessarily produces flawed results, but at the same time, this study highlights that it cannot be used as the standard model for every case scenario, since it may differ greatly from reality, as in the elastomers presented in this work. It does not mean either, that the disk-like geometry represents perfectly the reality. As was mentioned at the beginning, in reality the cavities of the polymers have an irregular shape, impossible to be represented with a simple geometry. Nonetheless this result is useful to better represent the microstructure of the elastomers that reflects their macroscopic behavior. Moreover, it emphasizes that the expansion of the holes must not always be equal in every direction of the space, but it could prefer a direction over the others. In future, in order to get a better understanding of the hole morphology in rubbers, computer simulations of the elastomers would be needed, but

this path is rather time consuming and It has to be guided by the awareness obtained from the results achieved so far.

Bibliography

[1]   R. Srithawatpong, Z. L. Peng, B. G. Olson, A. M. Jamieson, R. Simha, J. D. McGervey, T. R. Maier, A. E. Halasa and H. Ishida, *Journal of Polymer Science Part B: Polymer Physics,* no. 37, p. 2754, 1999.

[2]   S. G. Karshenboim, "Precision Study of Positronium: Testing Bound State QED Theory," *International Journal of modern Physics A,* pp. 9-10, 2003.

[3]   R. Simha and T. Somcynsky, *Macromolecules,* no. 2, p. 342, 1969.

[4]   K. Plotkowsky, T. J. Panek and J. Kansy, *Journal of Physics: Condensed Matter,* no. 6, p. 2643, 1994.

[5]   P. Winberg , M. Eldrup and F. H. J. Maurer, *Journal of Chemical Physics,* no. 136, 2012.

[6]   Y. Ito, H. F. M. Mohamed, K. Tanaka, K. Okamoto and K. Lee, *Journal of Radioanalytical and Nuclea Chemistry,* no. 211, p. 211, 1996.

[7]   J. Bartoš, O. Šauša, J. Krištiak, T. Blochowicz and E. Rössler, *Journal of Physics: Condensed Matter,* no. 13, 2001.

[8]   J. Bartoš, A. Alegría, O. Šauša, M. Tyagi, D. Gómez, J. Krištiak and J. Colmenero, *Physical Review Journal,* no. 76, 2007.

[9]   S. J. Tao, *The Journal of Chemical Physics,* no. 56, p. 5499, 1972.

[10]   M. Eldrup, D. Lightbody and N. J. Sherwood, *The Journal of Chemical Physics,* no. 63, p. 51, 1981.

[11]   G. Consolati, *The Journal of Chemical Physics,* no. 117, p. 7229, 2002.

[12]   B. G. Olson, T. Prodpran, A. M. Jamieson and S. Nazarenko, *Polymer,* no. 43, p. 6775, 2002.

[13]   D. Walsh and P. Zoller, Standard Pressure Volume Temperature Data for Polymers, Boca Raton, FL: CRC Press, 1995.

[14]   E. Yaynik, Thermo-volumetric properties of some rubbers and polymers: an experimental investigation, Politecnico di Milano, 2019.

[15]   P. A. Rodgers, *Journal od applied Polymer Science,* no. 48, p. 1061, 1993.

[16]   L. A. Utraki, *Journal of Polymer Science Part B: Polymer Physics,* no. 42, p. 2909, 2004.

[17]   R. Simha, P. S. Wilson and O. Olabisi, *Colloyd and Polymer Science,* no. 251, p. 402, 1973.

[18]   P. A. Rogers, *Journal of Applied Polymer Science,* no. 48, p. 1061, 1993.

[19]   R. Simha and P. S. Wilson, "Thermal Expansion of Amorphous Polymers at Atmospheric Pressure. II. Theoretical Considerations," *Macromolecules,* no. 6, p. 908, 1973.